SECTION I

RESEARCH IN PROGRESS

NUCLEAR REACTIONS -- EXPERIMENTAL

Delta Resonance Effects in High-Energy Gamma Ray Production

J. Clayton, W. Benenson, D. Krofcheck, D.J. Morrissey, T.K. Murakami, J. Stevenson, and J.S. Winfield

The large production cross section of high-energy gamma rays in heavy-ion reactions has lead to considerable efforts to understand the production mechanism.[1-7] Most of the experimental evidence so far indicates that the dominant mechanism is incoherent neutron-proton bremsstrahlung.

An interesting question is whether the elementary process for high-energy gamma ray production remains the same when the bombarding energy is increased. Prakash *et al.*,[8] pointed out that the direct photon decay of the delta resonance, $\Delta \rightarrow N + \gamma$, may be an important source of gamma rays for $E_\gamma > 140$ MeV. Using an approach that employs detailed balance, they calculated the thermal contribution to high-energy gamma ray creation. This type of approach explains, qualitatively, many features of pion production close to threshold. This method does not use the soft photon approximation, and can therefore be extended to much higher energies. Such an approach can investigate the influence of the delta isobar degree of freedom in photon creation.

The detailed balance model yields reasonable agreement with existing data, but it also predicts that the yield of gamma rays above E_γ = 140 MeV is enhanced by a factor of 5 to 10 times over the expected exponential fall-off. A calculation for the system ^{16}O+Ni is shown in Fig. 1 at E/A=44 and 95 MeV. Note that the predicted enhancement should be observable at E/A=44 MeV, but increases with increasing beam energy.

The objective of the present experiment is to investigate the gamma ray production cross section up to 200 MeV in order to search for gamma rays from the decay of the delta resonance.

A E/A=75 MeV ^{14}N beam from the K1200 cyclotron irradiated a self-supporting Zn foil of thickness 72 mg/cm^2. The high-energy gamma rays were measured by a 12.70 cm × 22.9 cm BaF_2 crystal placed 0.75 m from the target, and at 90° in the laboratory. The detector was collimated with a lead collimator to a diameter of 10.2 cm. Background radiation from charged particles was greatly diminished by the use of a 20-cm nylon absorber placed between the crystal and the target. Prompt neutrons from the target were also reduced by the nylon bar; however, the main method for neutron rejection relied on measuring the time-of-flight between the detector and the cyclotron rf timing. Plastic scintillators surrounding the detector rejected the background radiation from the cosmic rays.

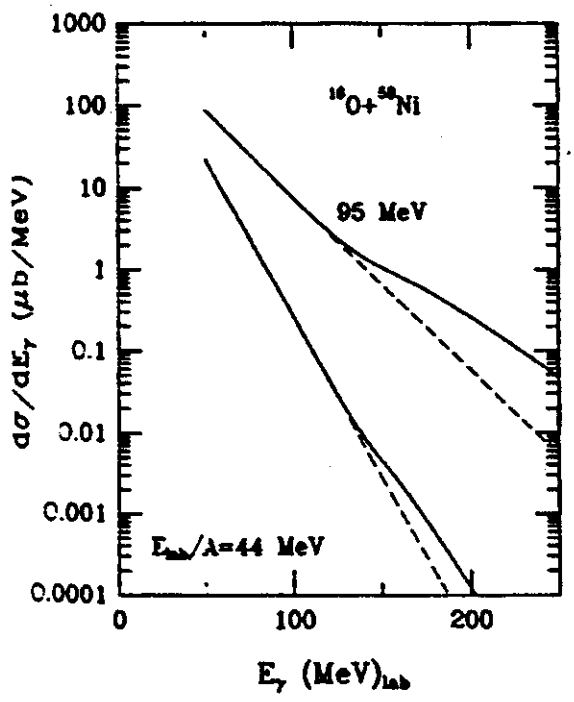

FIG. 1: Predicted gamma ray production cross sections from the model of Prakash et al.[8] The system is ^{16}O+Ni at E/A=44 and 95 MeV.

Figure 2 displays the measured spectrum of high-energy photons. In contrast to the prediction, shown in Fig. 1, the measured spectrum is well-represented by an exponential function up to E_γ=190 MeV . This shape is in qualitative agreement with other measured spectra for high-energy gamma ray production.[4,9,10] The full-scale energy is somewhat uncertain because the detector has not been calibrated with tagged photons. We estimated the full-scale

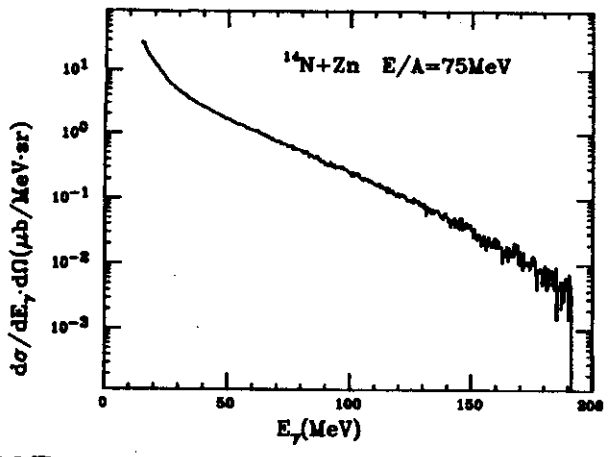

FIG. 2: The measured energy spectrum for high-energy gamma rays from the heavy-ion reaction ^{14}N+Zn at E/A=75 MeV.

energy by two methods: extrapolating the measured 15.1 MeV gamma ray transition in ^{12}C, and measuring the energy loss in the BaF_2 detector using cosmic ray muons. For the latter, we placed two 160 cm^2 scintillator paddles above and below the BaF_2 crystal, and demanded a triple coincidence. We found that the peak in the energy-loss spectrum for muons corresponds to approximately 98 MeV, which agrees with the extrapolation from the 15.1 MeV state in ^{12}C.

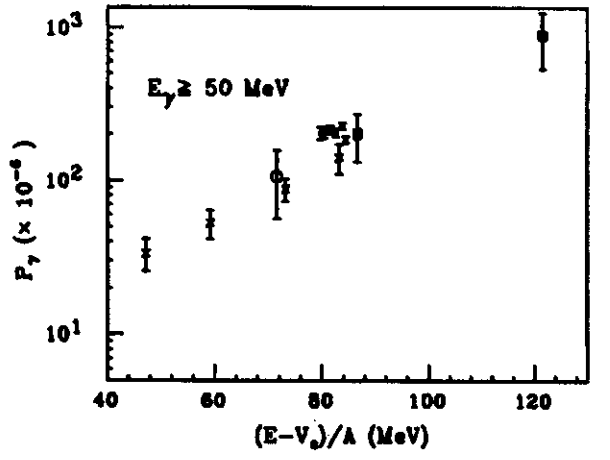

FIG. 3: Plot of probability of gamma ray emission P_γ, from (1) for gamma rays with $E_\gamma \geq 50$ MeV in the laboratory versus the Coulomb corrected bombarding energy. The open circle is the present data. Other values are: from Ref. 9, solid diamonds, Ref. 4, crosses; Ref. 10, solid squares.

The integrated cross section above $E_\gamma = 50$ MeV in the laboratory frame agrees with the previous data shown in Fig. 3, when it is scaled according to the equal participant model of Nifenecker and Bondorf.[6] Here, the probability of gamma ray emission, P_γ, is defined by:

$$\sigma_\gamma = \sigma_r < N_{np} > P_\gamma \qquad (1)$$

where $< N_{np} >$ is the impact parameter-averaged number of first neutron-proton collisions. The total reaction cross section, σ_r, is given by the geometrical cross section $\sigma_r = \pi(R_t + R_p)^2$.

The reason that we observed no significant enhancement in the gamma ray production cross section above $E_\gamma = 140$ MeV may be that the incident beam energy (E/A=75 MeV) is too low. It appears that the dominant mechanism is still incoherent neutron-proton bremsstrahlung rather than decay of the delta resonance. However, if the bombarding energy is further increased, it may be possible to see the effect of delta-resonance decay on direct photon production.

References

1. J. Stevenson *et al.*, Phys. Rev. Lett. 57, 555 (1986).
2. M. Kwato Njock *et al.*, Phys. Lett. 175B, 125 (1986).
3. N. Alamanos *et al.*, Phys. Rev. Lett. 173B, 392 (1986).
4. E. Grosse *et al.*, Europhys. Lett. 2, 9 (1986).
5. R. Hingmann *et al.*, Phys. Rev. Lett. 58, 759 (1987).
6. H. Nifenecker and J.P. Bondorf, Nucl. Phys. A442, 478 (1985).
7. W. Bauer, W. Cassing, U. Mosel and M. Tohyama, Nucl. Phys. A456, 159 (1986).
8. M. Prakash, P. Braun-Munzinger, J. Stachel, and N. Alamanos, Phys. Rev. C37, 1959 (1988).
9. M. Kwato-Njock *et al.*, Nucl. Phys. A489, 368 (1988).
10. J. Clayton *et al.*, (submitted to Phys. Rev. C).

High-Energy Gamma Rays from Reactions Induced by E/A = 15 MeV Heavy-Ion Beams

T.K. Murakami, W. Benenson, Y. Chen, J. Clayton,
E. Kashy, J. Stevenson, C.L. Tam, K. Hanold and M. Mohar

A significant yield of high-energy γ-rays were observed in recent experiments in which medium-energy heavy-ion collisions were studied.[1-4] Mechanisms which were proposed to explain these high energy photons include: nucleon-nucleon bremsstrahlung, coherent nucleus-nucleus bremsstrahlung, statistical decay, and nucleon bremsstrahlung in the nuclear potential field.

The dominant mechanism for beam energies higher than E/A = 44 MeV is believed to be bremsstrahlung produced by proton-neutron collisions. On the other hand, Herrmann *et al.*[5] claim that all of the high-energy γ-rays from the reaction of ^{92}Mo+^{92}Mo at E/A = 19.5 MeV can be accounted for by statistical decay. Since statistical decay is the dominant decay process of highly excited nuclei produced by low-energy heavy-ion reactions (E/A ≤ 10 MeV), it is expected that the two mechanisms will compete with each other in the energy range 10 ≤ E/A ≤ 20 MeV.

We report here measurements of the γ-ray production cross sections and angular distributions for symmetric and asymetric heavy systems, the ^{86}Kr+Zr, ^{40}Ar+Zr, and ^{40}Ar+Ca reactions, at E/A = 15 MeV. The gamma rays were measured with five 3"×3" BGO detectors, placed 0.7 m from the target at angles 40°, 60°, 90°, 120°, and 150°. The energy calibration for the detectors was performed with 15.1 MeV gamma rays produced in the ^{12}C+^{nat}C reaction at E/A = 20 MeV and with 4.44 MeV gamma rays from a Pu-Be source.

Eight 3"×3" NaI(Tl) detectors were set 0.65 m from the target at angles from 110° to 150° to measure the multiplicity of low-energy γ-rays in coincidence with high-energy photons.

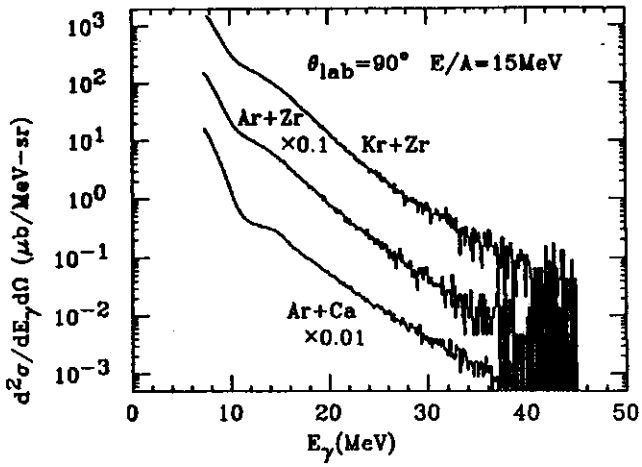

FIG. 1: γ-ray energy spectra measured by a BGO detector at 90° for three reaction systems at E/A = 15 MeV.

Figure 1 shows the spectra measured by the BGO detectors at 90° from the three reactions studied. The spectra exhibit three regions commonly observed with γ-rays:

1) below 11 MeV a steep decrease with increasing γ-ray energy,
2) a bump around 15 MeV due to the giant resonance in excited nuclei, and
3) an exponential region above 20 MeV. The γ-rays in region 3 are the subject of this report.

The measurement of γ-ray angular distributions gives the source velocity, and hence provides a good test of various models of high-energy γ-ray production. If the source of the gamma rays is first-collision nucleon-nucleon bremsstrahlung, the source is the nucleon-nucleon center-of-mass frame. If, on the other hand, the source of the γ-rays is statistical emission from a compound nucleus, or two nuclei following a deep inelastic collision, the source velocity is the nucleus-nucleus center of mass.

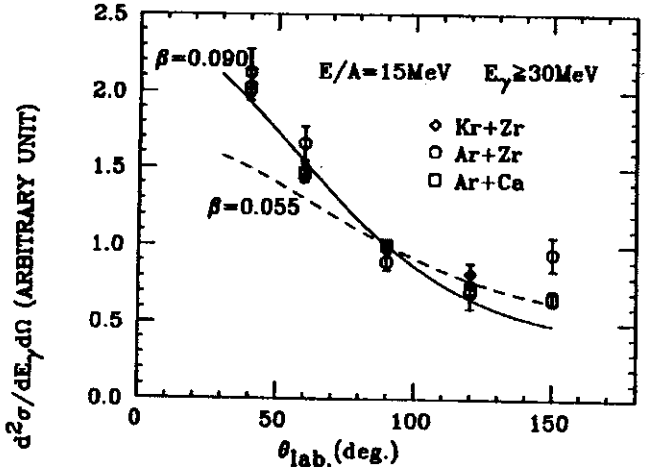

FIG. 2: Angular distributions in the laboratory frame. The solid line and the dashed line correspond to estimated results for isotropy in a frame with $\beta = 0.090$, and 0.055, respectively.

Figure 2 shows the measured angular distributions for the three reactions in the laboratory frame. All three reactions show a similar shape for angular distributions, with a peak at forward angles. The solid line represents the calculated distribution for isotropic emission of γ-rays in a frame moving with the velocity of the nucleon-nucleon center-of-mass frame ($\beta = 0.090$). The experimental results are in good agreement with the solid line. Since the $^{86}Kr+Zr$, and $^{40}Ar+Ca$ reactions are nearly mass-symmetric, the nucleon-nucleon and nucleus-nucleus center-of-mass frames have almost the same velocity.

The nucleus-nucleus center of mass frame of the $^{40}Ar+Zr$ reaction has a different velocity. The dashed line represents an angular distribution that is isotropic in a frame moving at $\beta = 0.055$, the velocity of the nucleus-nucleus center of mass frame for the $^{40}Ar+Zr$ reaction. The angular distribution of the $^{40}Ar+Zr$ reaction is better represented by a transformation to the nucleon-nucleon center-of-mass frame. Thus the nucleon-nucleon first-collision model is consistent with all the angular distributions in the experiment.

The γ-ray multiplicity was measured by observing coincidences between the small NaI(Tl) detectors and high-energy photons. All the spectra were added together because they showed an identical shape with an exponential fall-off up to the maximum energy of 6 MeV. The multiplicity was calculated from the ratio of coincidence-to-singles events, using the solid angles and calculated total efficiency of the small NaI(Tl) detectors. The multiplicity is shown in Fig. 3 as a function of photon energy detected in the BGO detectors.

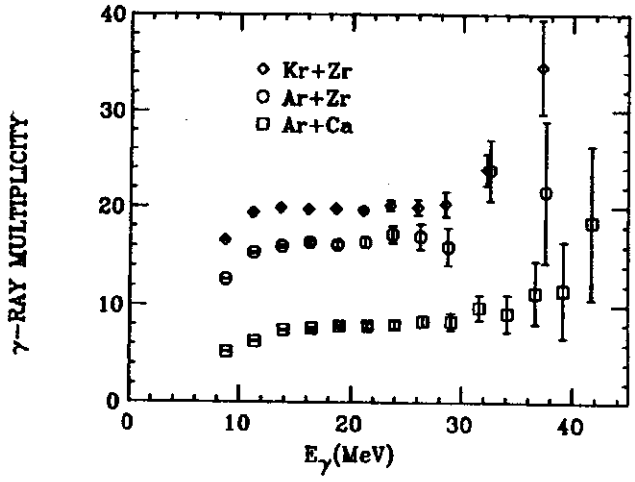

FIG. 3: γ-ray multiplicity as a function of high-energy gamma-ray energy. The error bars are only statistical. The multiplicity M_γ includes the high-energy photon detected by the BGO detectors.

Several features are apparent in Fig. 3. First, the multiplicity depends on the reaction, and increases with increasing mass of the target and projectile. Second, the multiplicity between $E_\gamma = 14$ and 28 MeV is almost constant. Third, a slight increase in the multiplicity may exist above $E_\gamma = 30$ MeV.

Deep inelastic collisions are thought to be the dominant reaction of $^{86}Kr+Zr$ at $E/A = 15$ MeV. Using the average angular momentum of the entrance channel, the intrinsic angular momentum of the $\langle L_i \rangle$ of the two fragments can be estimated to be about $63\hbar$ at the rolling limit. The corresponding value of the multiplicity is $\langle M_\gamma \rangle = 28$ to 30, according to the relation between the average angular momentum and γ-ray multiplicity reported in Ref. 6. The observed multiplicity is smaller than the expected value in the region below 35 MeV. The ^{40}Ar-induced reactions are more complicated, since fusion-like residues are thought to be abundant. The same procedure gives $24\hbar$ and $37\hbar$ ($\langle M_\gamma \rangle = 6$ and 15) for the $^{40}Ar+Ca$ and $^{40}Ar+Zr$ reactions, respectively, which are more consistent with the observed values below $E_\gamma = 30$ MeV.

References

1. J. Stevenson *et al.*, Phys. Rev. Lett. 57, 555 (1986).
2. E. Grosse *et al.*, Europhys. Lett. 2, 9 (1986).
3. M. Kwato Njock *et al.*, Phys. Lett. B175, 125 (1986).
4. R. Hingmann *et al.*, Phys. Rev. Lett. 58, 759 (1987).
5. N. Herrmann *et al.*, Phys. Rev. Lett. 60, 1630 (1988).
6. M.N. Namboodiri *et al.*, Phys. Rev. C20, 982 (1979).

Non-Equilibrium Versus Equilibrium Emission of Complex Fragments From Hot Nuclei

D.E. Fields[a], K. Kwiatkowski[a], D. Bonser[b], R.W. Viola[c] and V.E. Viola, W.G. Lynch, J. Pochodzalla[d], M.B. Tsang, C.K. Gelkbe, D.J. Fields[c], and S.M. Austin

The emission of intermediate mass fragments (IMF: fragments heavier than α-particles, but lighter than fission fragments) occurs with appreciable yields for nuclear systems at high excitation energy, E≥ 100 MeV, and presents a problem of great current interest in the study of macroscopic nuclear behavior.[1,2]

It is best studied back of the grazing angle where contributions from quasi-elastic projectile fragmentation reactions are negligible. Measurements indicate that intermediate mass fragments are emitted from highly excited target-like sources.[1-7] The fragments exhibit Maxwell-Boltzmann-like kinetic energy spectra with maxima near the Coulomb energy for touching spheres. The angle-integrated cross sections obey an approximate power-law dependence on the fragment mass, $\sigma \propto A^{-\tau}$, independent of projectile mass.[5]

For nuclear reactions at low and intermediate energies, fragment emission at backward angles has been attributed to the decay of fully equilibrated systems.[3] Fragment emission at forward angles occurs through non-equilibrium processes,[6,7] as evidenced by forward-peaked angular distributions, negative angle scattering,[8] and shapes of the kinetic energy spectra inconsistent with compound nucleus emission.[1,2,6]

The decomposition of the intermediate mass fragment cross sections into non-equilibrium and equilibrium contributions is essential for any quantitative understanding of either process. Here, we describe a systematic evaluation of the relative importance of equilibrium and non-equilibrium fragment emission processes as a function of incident energy for ^{14}N-induced reactions on Ag and Au targets at projectile energies of E/A=20-50 MeV. These measurements indicate that non-equilibrium processes increasingly dominate the intermediate mass fragment cross sections as the incident energy is increased.

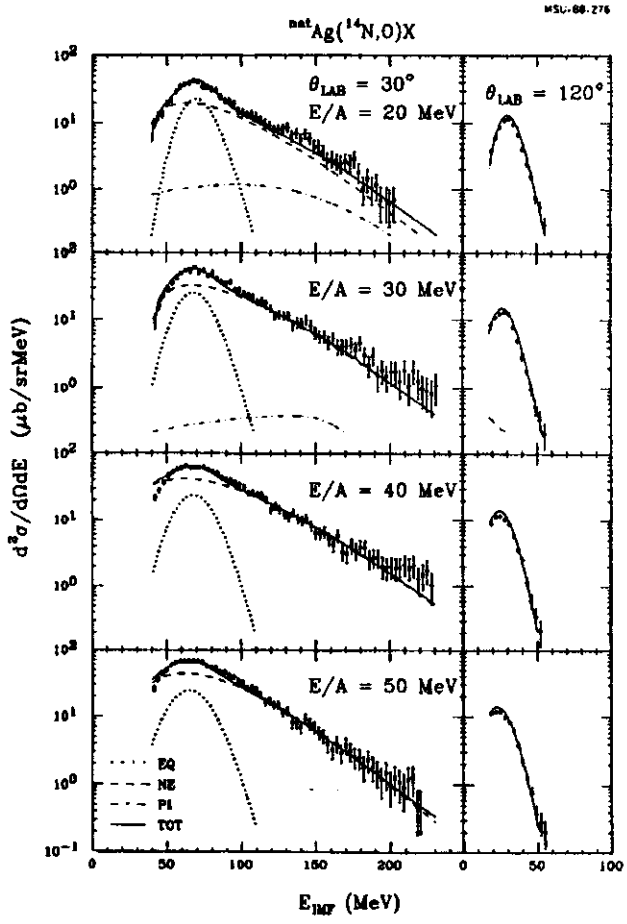

FIG. 1: Laboratory kinetic energy spectra for oxygen fragments emitted in ^{14}N+^{nat}Ag reactions at E/A=20, 30, 40, and 50 MeV. The left- and right-hand parts show spectra measured at θ_{lab}=30° and 120°, respectively. The solid lines represent fits with three sources: equilibrium and non-equilibrium emission from the target-like source are shown by the dotted and dashed curves, respectively. Emission from the projectile-like source is indicated by the dot-dashed curves.

The experiments were performed at the NSCL. Beams of E/A=20, 30, 40, and 50 MeV ^{14}N ions from the K500 MeV cyclotron bombarded high purity targets of Ag and Au. Particle telescopes, placed at laboratory angles of 60°,

90°, 120° and 165°, each consisted of an axial-field gas-ionization chamber, followed by a totally depleted 300-μm silicon surface barrier detector and a 5-mm lithium-drifted silicon detector. At forward angles, Θ_{lab} = 20°-40°, the measurements were performed with a telescope consisting of three planar surface-barrier silicon detectors of thicknesses 30μm, 100μm and 400μm, respectively, followed by a 5-mm thick lithium-drifted silicon detector.

Representative fragment kinetic energy spectra and angular distributions are shown in Figs. 1 and 2, respectively. At backward angles the kinetic energy spectra exhibit steep slopes, consistent with equilibrium emission from residues formed in incomplete fusion reactions; at intermediate angles the spectral slopes become less steep, indicating strong contributions from non-equilibrium emission (see Fig. 1). At forward angles near the grazing angle, an additional high-energy component appears in the spectra of lighter fragments ($Z \leq 8$). This component (barely visible in the 30° spectra shown in Fig. 1) is attributed to peripheral reactions, i.e. projectile fragmentation, inelastic scattering, or transfer reactions. Consistent with previous observations, the slopes of the energy spectra do not exhibit a marked dependence on projectile energy.

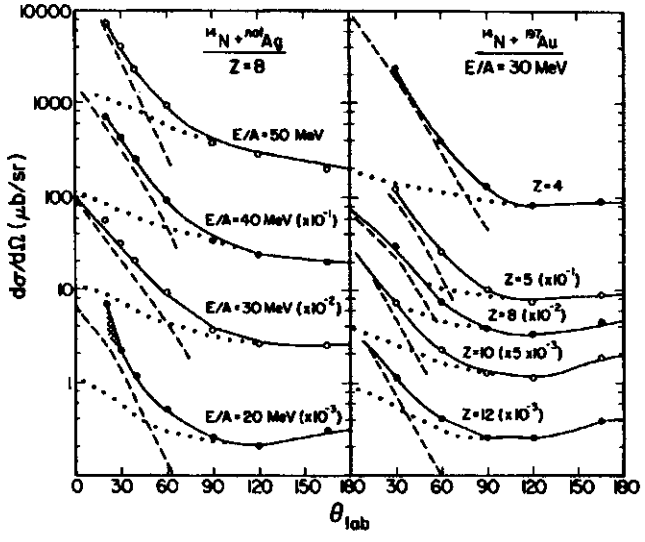

FIG. 2: Examples of angular distributions in the laboratory frame of reference. Part (a) shows angular distributions for oxygen fragments emitted in reactions on ^{nat}Ag at E/A = 20, 30, 40, and 50 MeV; part (b) shows angular distributions for fragments with different element numbers Z emitted in reactions on ^{197}Au at E/A = 30 MeV. The dotted and dashed lines show equilibrium and non-equilibrium contributions from the target-like source, respectively; the solid line represents the sum of all three sources. The cross-hatched region designates the contribution from projectile-like fragments produced in peripheral reactions.

The laboratory angular distributions shown in Fig. 2 are relatively flat for heavier fragments. In some cases, particularly at lower energies and for the heaviest fragments, they exhibit a slight rise at back angles. Forward angle contributions from projectile-fragmentation reactions are significant at E/A = 20 MeV, but decrease in importance rapidly at higher energies and for angles greater than 20°.

In order to assess the relative importance of equilibrium and non-equilibrium emission, we have fitted the spectra for each fragment by assuming contributions from two target-like sources and a third source to account for contributions from peripheral reactions at forward angles. Representative fits and the relative contributions of each component are shown by the curves in Figs. 1 and 2.

The sources representing equilibrium emission (shown by the dotted curves) were assumed to be stationary in the rest frame of the target-like residue; they were characterized by their mean velocities, v_{EQ}, Coulomb barriers, B_{EQ}, and temperatures, T_{EQ}. The spectral shapes were parametrized according to the model of Moretto.[10] The equilibrium angular distribution functions were taken to be symmetric about 90° in the emitting-source frame with the angular anisotropy parametrized as $(1 + \beta \cdot \cos^4\Theta)$ where β is a fit parameter.

Non-equilibrium emission from the target-like source was described by a Maxwellian distribution characterized by "kinetic temperature" parameters, T_{NEQ}, mean source velocities, v_{NEQ}, and Coulomb barriers, B_{NEQ}. An angular distribution function, $W(\Theta) \propto \exp(-\alpha\Theta)$, was employed in the fitting of this source. This contribution is shown by the dashed lines in Figs. 1 and 2. The projectile-like third source was parametrized according to the prescription of Kiss *et al.*[13] This source was important primarily at the very forward angles for fragments with $Z \leq 8$ at E/A = 20 MeV; it is indicated by the dot-dashed line in Fig. 1.

Fits to the data were performed in two steps. In the first step, equilibrium source temperatures and spectral shape parameters were determined by fitting only data at backward angles. The fit temperatures were found to be close to those expected for residual nuclei formed in fusion-like reactions. These parameters were then kept fixed in the

global fits with all three sources performed in the second step. The fitted equilibrium source velocities evolved systematically over the range $v_{EQ} \approx 0.7\text{-}1.0 \cdot v_{CN}$, where v_{CN} is the velocity of the compound nucleus formed in a complete fusion event. Source velocities closest to v_{CN} were obtained for heavy fragments and low bombarding energies; smaller values were found for light fragments and high bombarding energies. These results are qualitatively consistent with linear momentum transfer measurements of similar systems.[11,12]

Values of the equilibrium and non-equilibrium cross sections, σ_{EQ} and σ_{NEQ} respectively, for the target-like source were determined by integrating the corresponding fitting functions over all energies and over the angular range of $\theta_{lab} = 5° \text{-} 180°$. Total IMF cross sections for the target-like source, σ_{IMF}, were then determined from the sum of σ_{EQ} and σ_{NEQ}.

The decomposition of the IMF cross sections from the target-like source into a single equilibrium and a single non-equilibrium component represents a strong simplification, since more than two distinct sources may contribute to the inclusive cross sections. This definition has the practical effect of defining equilibrium emission in terms of processes for which the intera ction time is greater than approximately one rotation period. Our operational definition of the equilibrium component based on the back-angle data corresponds to a necessary, but not sufficient condition for emission from fully equilibrated systems; it therefore provides only an upper limit for σ_{EQ}. For example, σ_{EQ} is overestimated if these backward-angle data include significant contributions from non-equilibrium emission mechanisms. Also, use of a third projectile-like source has the effect of lowering the derived values of σ_{NEQ}.

Figure 3 shows the energy dependence of the extracted ratios, $\sigma_{NEQ}/\sigma_{IMF}$, for fragments of even element numbers Z. (The results for fragments with odd values of Z are similar; for example, the measured and the fitted Li/Be cross section ratios are approximately 3 for all cases measured in this experiment, leading to the same fraction of non-equilibrium emission for the two elements.) As could already be seen from the qualitative features of the angular

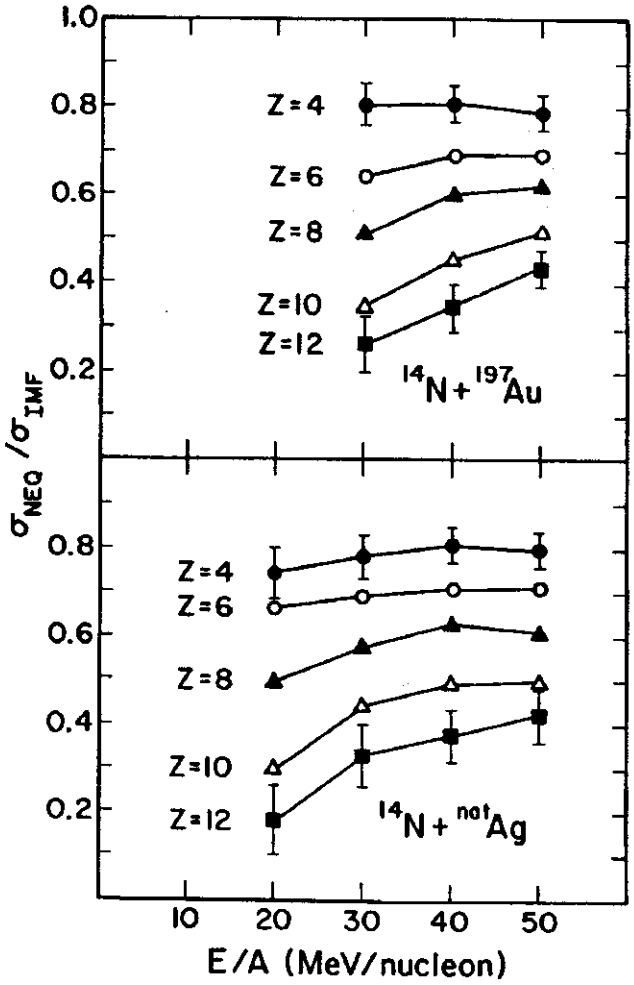

FIG. 3: Minimum fraction, $\sigma_{NEQ}/\sigma_{IMF}$, of IMF cross sections due to non-equilibrium emission. The upper and lower panels show results for ^{197}Au and ^{nat}Ag targets, respectively. Representative systematic errors are shown for Z=4 and 12 fragments.

distributions, complex fragment emission at low energies includes important contributions from both equilibrated and nonequilibrated sources. With increasing bombarding energy, non-equilibrium emission grows in importance. In general, non-equilibrium emission is favored for light fragments.

The trends in the ratio $\sigma_{NEQ}/\sigma_{IMF}$ are very similar for both targets, with somewhat lower values observed for heavier fragments emitted in reactions on gold. The energy- and mass-dependent trends of the lower limits on $\sigma_{NEQ}/\sigma_{IMF}$ presented in Fig. 3 are largely insensitive to details of the parametrizations adopted in our analysis. Systematic errors shown in the figure were estimated by using different prescriptions to extract the equilibrium and non-

equilibrium contributions; they reflect, in part, the uncertainties of extrapolating the experimental cross sections to forward angles. The largest uncertainties occur at the lowest bombarding energies for fragments with $Z \leq 7$ where contributions from peripheral reactions blur the distinction between target-like and projectile-like sources at forward angles.

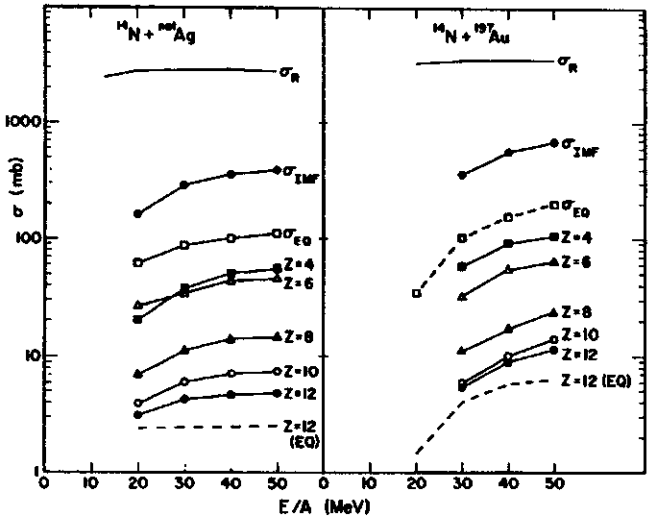

FIG. 4: Excitation functions for cross sections, σ_{IMF}, corresponding to the emission of IMF's with even Z; the summed IMF cross sections, $\sum\sigma_{IMF}$ and $\sum\sigma_{EQ}$, and the calculated reaction cross sections, σ_R.

Figure 4 presents the excitation functions for fragments with even Z. For the ^{14}N+Au reaction at E/A=20 MeV, only the equilibrium cross sections are presented, since only one forward angle was measured for this system and strong contributions from transfer and projectile fragmentation components prevented reliable estimates of the non-equilibrium cross sections. Also shown are the IMF cross sections summed over Z=3-12, $\sum\sigma_{IMF}$ and $\sum\sigma_{EQ}$, and the calculated values[14] of the total reaction cross section, σ_R.

The excitation functions are slightly different for the two target-projectile combinations, with cross sections for gold exhibiting slightly more pronounced energy dependences and slightly larger values at higher energies. The IMF cross sections increase slowly above energies of E/A≈30 MeV and have not reached a limiting value at E/A=50 MeV. For the Ag target, the increase at higher energies is somewhat slower than for the Au target; this is true for both σ_{IMF} and σ_{EQ}. The small values of the summed IMF cross sections, $\sum\sigma_{IMF}$, imply that less than one fragment is emitted per average collision. Coincidence measurements performed at higher energies will be needed to clarify whether, for specific collisions, the fragment multiplicities will exceed unity, as could be expected for a multiple sequential emission of heavy fragments and/or multifragmentation processes.

References

a. Indiana University Cyclotron Facility, Indiana University, Bloomington, IN 47405

b. Department of Chemistry, University of Washington, Seattle, WA 89185

c. Lawrence Livermore Laboratory, Livermore, CA 94550

d. Universität Frankfurt, D-6000 Frankfurt, Fed. Rep. Germany

e. Pritzger School of Medicine, University of Chicago, Chicago, IL 60637

1. W.G. Lynch, Annu. Rev. Nucl. Sci. 37, 493 (1987).

2. "Proceedings of the Symposium on Central Collisions and Fragmentation Processes," edited by C.K. Gelbke, Nucl. Phys. A471, 1-451c (1987).

3. L.G. Sobotka *et al.*, Phys. Rev. Lett. 51, 2187 (1983).

4. A.M. Poskanzer *et al.*, Phys. Rev. C3, 882 (1971).

5. R.W. Minich *et al.*, Phys. Lett. 118B, 458 (1982); J.E. Finn *et al.*, Phys. Rev. Lett. 49, 1321 (1982).

6. D.J. Fields *et al.*, Phys. Rev. C30, 1912 (1984); Phys. Rev. C34, 536 (1986).

7. K. Kwiatkowski *et al.*, Phys. Lett. B171, 41 (1986).

8. M.B. Tsang *et al.*, Phys. Rev. Lett. 60, 1479 (1988).

9. R. Trockel *et al.*, Prog. Part. Nucl. Phys. 15, 225 (1985).

10. L.G. Moretto, Nucl. Phys. A247, 211 (1975).

11. M.B. Tsang *et al.*, Phys. Lett. B176, 169 (1984); M. Fatyga *et al.*, Phys. Rev. Lett. 55, 1376 (1985).

12. M. Fatyga *et al.*, Phys. Rev. Lett. 58, 2527 (1987).

13. A. Kiss *et al.*, Michigan State University Report MSUCL-650, 1988.

14. S. Kox *et al.*, Nucl. Phys. A420, 162 (1984).

Light Fragments from ^{14}N + Ag Reactions at E/14 = 35 MeV

F. Deák,[a] A. Kiss,[a] Z. Seres,[b] A. Galonsky, and L. Heilbronn

Velocity spectra of fragments and of neutrons in coincidence with them have been determined from ^{14}N + Ag collisions at 35 MeV/nucleon.

Analysis of neutron spectra having various fragment gates with two moving sources reveals an intermediate rapidity source with temperatures of 10.2 ± 1.6 MeV and velocities corresponding to E/A of 10.7 ± 2.0 MeV/nucleon and a slowly moving, target-like source whose temperatures and E/A values lie in the ranges 2.0-3.6 MeV and 0.1-0.3 MeV/nucleon, respectively, for both the quasi-elastic and the deep-inelastic events.

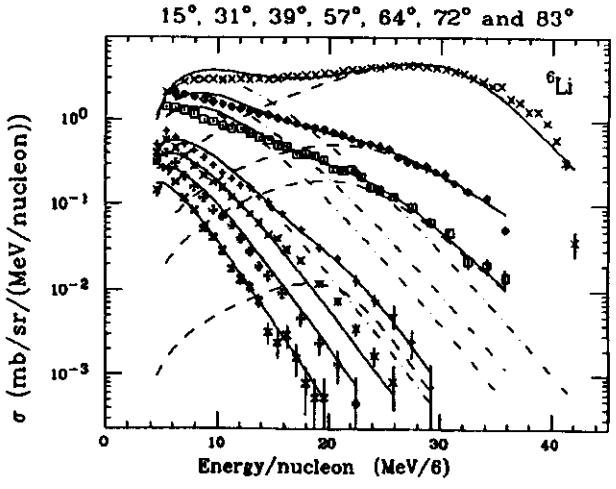

FIG. 1: Spectra of ^{6}Li fragments at (from top to bottom) 15°, 31°, 39°, 57°, 64°, 72°, and 83°. Each dashed line is a fit to the quasi-elastic part; each dot-dashed line is a one-moving-source fit to the remaining (deep-inelastic) part; and each solid line is the sum of the two contributions.

Fragment velocity (actually velocity squared) spectra were constructed at seven angles from 15° to 83° for isotopes of ^{6}Li, ^{7}Li(+^{8}Be), ^{7}Be, ^{9}Be, ^{10}Be, ^{10}B, ^{11}B, ^{12}B, ^{11}C, ^{12}C, ^{13}C, ^{14}N, and ^{15}N. A typical set of these spectra, here for ^{6}Li, is displayed in Fig. 1. The spectral shapes for the other isotopes are similar to those in Fig. 1, although the exponential fall-offs at the larger angles are steeper in the spectra of the heavier fragments. The spectra at the four most forward angles in Fig. 1 were fitted with a two-component model, a quasi-elastic (QE) component and a deep-inelastic (DI) component. The QE component has an empirical prescription. Its strength falls off rapidly with angle and is negligible beyond 57°. For heavier fragments it becomes negligible at smaller angles, but it is always dominant at 15°. The DI component has the standard parameterization of a hot moving source.

Table I contains the values of the fit parameters--σ, the source strength; E/A, the source velocity (squared); and T, the source temperature. The table shows that for DI fragment production neither the velocity nor the temperature parameter deviates much from isotope to isotope, although there is a slight increase in both values from ^{6}Li to ^{15}N. This similarity suggests that a single mechanism is responsible for the production of most of the DI fragments. A moving source origin would be quite in the spirit of our investigation. And Table I gives the parameter values of such a source.

TABLE I. Parameters of the moving source fits (σ: production cross section; T: temperature) and the weighted neutron/proton ratios (N/Z) for the deep-inelastic component. The statistical deviations for the parameters are less than 10%.

Fragment	σ (mbarn)	E/A (MeV/nucl)	T (MeV)
^{6}Li	49.9	3.81	11.4
^{7}Li	79.7	3.65	11.6
^{7}Be	15.3	4.66	12.7
^{9}Be	16.5	3.41	11.9
^{10}Be	9.46	3.37	12.4
^{10}B	11.6	3.89	13.2
^{11}B	21.8	3.44	12.6
^{12}B	3.00	3.36	12.8
^{11}C	2.65	4.43	14.5
^{12}C	9.30	4.17	13.3
^{13}C	6.75	4.27	13.1
^{14}N	2.17	4.23	13.7
^{15}N	4.27	4.34	12.6
Averages		3.9±0.5	12.8±0.9

However, there is a physical inconsistency. Looking at Table II, in which the average source temperature and velocity parameters are gathered, we see that the velocity of the DI fragment source is much lower than the neutron source velocities. The inconsistency is that it is hard to imagine a hot source that does not emit neutrons. Yet the neutron analyses, while producing sources of about the same temperature, had them moving much faster, at approximately half the beam velocity. Perhaps this means that a thermal source fit to the DI fragment data, while mathematically valid, does not represent a physically real equilibrium emission. As we cannot identify a neutron source with the parameters of the fragment source, the actual origin of the deep-inelastic fragments may be a non-equilibrium process such as occurs in the stripping-pickup model.[1-3]

Table II. Average temperature and velocity parameters of the moving sources.

Source	Temperature (MeV)	E/A (MeV/nucleon)
Neutrons:		
Quasi-elastic (QE)	10.4±1.6	11.0±2.1
Deep inelastic (DI)	10.0±1.5	10.5±2.0
Fragments:		
Deep inelastic (DI)	12.8±0.9	3.9±0.5

This model assumes that a hot participant source develops in the interaction of an abraded part of the projectile with an approximately equal mass from the target nucleus. The source emits the IR neutrons (and protons). Later the coincident fragment is formed in a decelerating mass pickup by the projectile spectator from the source.

The general idea of a QE fragment being produced by a projectile fragmentation and a subsequent interaction with the created hot zone is supported by a recent experiment on ^{12}B fragments.[4] In that experiment it was seen that the highest energy QE fragments are cold, and they become gradually more excited as the kinetic energy of the ^{12}B fragment decreases.

The stripping-pickup model is a non-equilibrium model. It gives a qualitative description of the shape of the QE fragment spectrum. The peak in such a spectrum, the 15° spectrum of Fig. 1, for example, is just below the velocity of the projectile, and it has a low-velocity tail. In the model the projectile splits into a part that creates a hot zone in the target and a spectator part that becomes the fragment after it picks up some nucleons in a decelerating interaction with the hot zone. The more nucleons picked up, the more deceleration and, since the single nucleon pick-up probability is small, the smaller the probability. Hence, the low-velocity tail.

By symmetry of nucleus-nucleus collisions in the CM system, we can expect reactions in which the target splits and in the same way the spectator part, after some interaction, becomes the fragment. In this case, however, the spectator that interacts very little is left almost at rest in the laboratory. Spectator interactions that pick up several nucleons are less probable, but the greater interaction drags them along with the forward moving hot zone, imparting a higher velocity in the laboratory. Hence, the decreasing, almost exponentially falling DI spectrum.

Another observation explained by this model is that the DI fragments are more isotropically distributed in the forward hemisphere than are the QE events--a simple consequence of the kinematics of the model. The model also predicts that the internal excitation of the fragment should depend on the velocity of the fragment. In this picture the DI fragments with the lower velocities are those that interacted less with the hot zone. The lower velocity DI fragments would, therefore, be colder than the more energetic ones. (The opposite would be true of QE fragments.) Just such an effect has been reported in ^{14}N + Au collisions at 35 MeV/nucleon[5] and in ^{16}O + Ag and ^{32}S + Ag collisions at 30 MeV/nucleon. Finally, the proposed model is a non-equilibrium model of fragment emission. Evidence for excited fragments with non-equilibrium state populations[7] was recently found in the same system as ours, ^{14}N + Ag at E/A = 35 MeV. The finding of non-equilibrium is in agreement with that feature of our model.

References

a. Eötvös Lourand University, Budapest, Hungary

b. Central Research Laboratory for Physics, Budapest, Hungary

1. A. Kiss *et al.*, Nucl. Phys. A499, 131 (1989)

2. F. Deák *et al.*, Nucl. Phys. A464, 133 (1987)

3. A. Kiss *et al.*, Phys. Rev. C38, 170 (1988)

4. F. Deák *et al.*, Phys. Rev. C39, 733 (1989)

5. C.B. Chitwood *et al.*, Phys. Lett. B172, 27 (1986)

6. R. Wada *et al.*, Phys. Rev C 497 (1989).

7. K.T. Nayak *et al.*, Phys. Rev. Lett. 62, 1021 (1989)

Complex Fragments Emitted in Particle-Stable States for the $^{32}S + ^{nat}Ag$ Reaction at E/A = 22.3 MeV

H.M. Xu, W.G. Lynch, C.K. Gelbke, M.B. Tsang, D.J. Fields[a], M.R. Maier, D.J. Morrissey, T.K. Nayak, J. Pochodzalla, D.G. Sarantites[b], L.G. Sobotka[b], M.L. Halbert[c], and D.C. Hensley[c]

Measurements of the relative populations of nuclear states can provide information about the internal excitation during the late stage of the reaction and can be used to extract an "emission temperature" for the ensemble of emitted fragments.[1-11] If the populations of states could be described in terms of thermal equilibrium distributions corresponding to a single emission temperature, this temperature could be unambiguously determined by measuring the relative populations of only two states. On the other hand, the degree of thermalization and the internal consistency of thermal assumptions can only be investigated by measuring a large number of states. Unfortunately, all previous temperature measurements using relative populations of excited states[1-11] were based on only a few states, and the degree of thermalization, as well as the thermal assumptions, could not be addressed.

To provide such a test, we measured the γ-ray decays of a large number of high-lying particle-stable states of intermediate mass fragments for ^{32}S induced reactions on ^{nat}Ag at the incident energy of E/A = 22.3 MeV.[12] These measurements were performed at angles back of the grazing angle to avoid large contributions from peripheral processes.

The experiment was performed at the Holifield Heavy-Ion Research Facility of Oak Ridge National Laboratory. Silver targets of natural isotopic abundance were irradiated with ^{32}S ions of 715 MeV energy. Intermediate mass fragments were isotopically identified with five ΔE-ΔE-E surface barrier detector telescopes, positioned at the laboratory angles of θ_{lab} = 20°, 25°, 30°, 45° and 50°, with solid angles of $\Delta\Omega$ = 9.8, 10.1, 15.4, 36.3, and 28.6 msr, respectively. Each telescope consisted of two planar ΔE-detectors with thicknesses between 50 and 100μm and an E-detector 1.5 mm thick. Cross contamination between adjacent isotopes was reduced by restricting the analysis to fragments that stopped in the E-detectors of the telescopes, thus permitting two independent particle identification gates. This introduced energy thresholds at about E/A = 8 MeV for θ = 20°, 25°, 30° and at about E/A = 7 MeV for θ = 45° and 50°.

Coincident γ-rays were detected with the NaI(Tl) modules of the Spin Spectrometer.[13] Spectra measured with detectors located in the forward hemisphere of the Spin Spectrometer were strongly contaminated by a background of fast, non-compound neutrons. To reduce the systematic errors arising from background subtraction, only NaI(Tl) modules were used, which were located in the backward hemisphere. For these detectors, significant reductions of the neutron background could be achieved by time-of-flight discrimination.

The energy spectra of coincident γ-rays were transformed, event by event, into the rest frames of the detected fragments, using relativistic Jacobian and Doppler shift corrections. Since these transformations shift and broaden γ-ray transitions of the target residues, particular attention was paid to identifying and correcting for such effects. For this purpose, background spectra were generated by performing similar transformations to γ-ray spectra, measured in coincidence with ^{9}Be nuclei, which have no strong transitions at the γ-ray energies of interest. Taking this background into account, the resulting coincidence yields were fitted by folding the detector response function with the energies of known transitions of the detected fragments and adjusting their relative strengths.

The detector response function was calibrated over the energy range of E ≈ 0.5 to 7 MeV with γ-rays emitted from ^{24}Na, ^{60}Co, ^{88}Y, ^{207}Bi radioactive sources, as well as γ-rays produced by the inelastic scattering of protons from ^{12}C and

^{16}O target nuclei.[12] The inclusive fragment yields and the fragment-γ-ray coincidence yields were summed over angle to extract the fraction, F_γ, of observed fragments which were accompanied by the designated γ-ray.

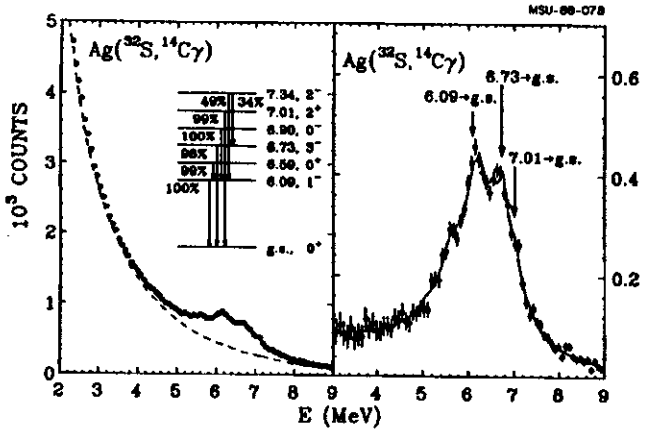

FIG. 1: γ-ray spectra measured in coincidence with ^{14}C fragments. The left-hand panel shows the raw coincidence spectrum with the background indicated by the dashed line. The right-hand panel shows the spectrum associated with γ-ray decays of excited ^{14}C fragments (with the background involving the decays of target residues subtracted). The solid line shows the fit used for the extraction of the γ-ray fractions, F_γ. Photopeak locations of important transitions or groups of transitions are indicated by arrows.

As an example, the solid points and dashed lines in the left-hand panel of Fig. 1 show the transformed coincidence and background spectra, respectively, for the case of ^{14}C fragments, summed over all measured particle emission angles and energies and over all γ-ray detectors located in the backward hemisphere. The solid points in the right-hand panel of Fig. 1 show the background subtracted spectrum. The solid lines represent the response function fits used for the extraction of individual transition strengths.

The hatched horizontal bands in Fig. 2 show the measured ratios, $R_\gamma = F_{\gamma 1}/F_{\gamma 2}$, of γ-ray transition probabilities for the fragments for which more than one transition could be reliably extracted. The solid lines represent sequential decay calculations which include feeding from higher-lying particle-unbound states, both discrete states[14] and continuum states.[12,15] In the calculations, the states of primary populations of fragments were assumed to be populated according to a thermal distribution characterized by a temperature, T.

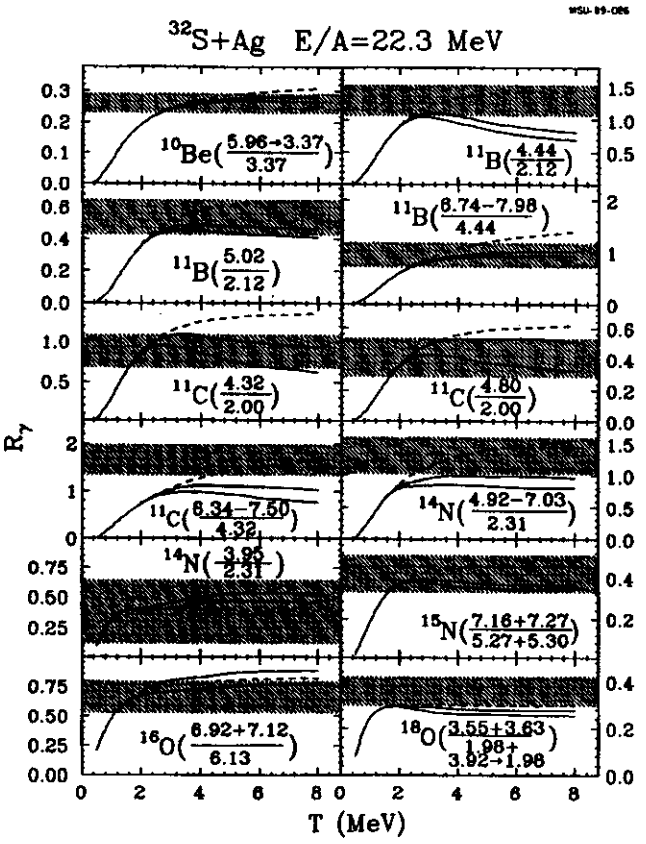

FIG. 2: The solid curves indicate the range of calculated ratios, $R_\gamma = F_{\gamma 1}/F_{\gamma 2}$, of designated γ-ray transition probabilities as a function of the emission temperature, T, which characterizes the ensemble of emitted fragments. (The values for R_γ on the curves are one theoretical standard deviation from the average value of R_γ provided by the calculations.) The dashed lines show the ratios calculated when feeding from particle-stable states is included, but not feeding from particle-unbound states. The horizontal bands indicate the measured values.

The decays of excited primary fragments were calculated using available information[14] concerning the spins, excitation energies and branching ratios of the individual states while particle decay branching ratios were not available, they were calculated from the statistical model.[16]

In contrast to previous calculations, higher-lying continuum states, up to excitation energies of $E_{cutoff} = \mu \cdot A$ for a given fragment of mass A, were included in the primary populations. This cutoff was introduced to explore the sensitivity of the calculations to the highly excited but short-lived nuclei, some of which may be too short-lived to survive the evolution from breakup to freezeout. In addition, while the spins, isospins, and parities for the low-lying discrete states were unknown, they were assigned randomly, according to a primary distribution obtained from a non-

interacting shell model,[17] and the calculations were repeated until the sensitivities of the populations to these uncertainties could be assessed. Finally, the parity and isospin conservation were enforced for decays of particle-unstable states. The uncertainties for calculations with μ = 3 MeV were demonstrated by the upper and lower solid lines in Fig. 2 (μ = 5 MeV were qualitatively similar).

In general, the experimental data are larger than the calculations for emission temperatures less than 2 MeV. For most transitions, the calculations are within 20% of the data for temperatures of about 3 to 4 MeV. However, at these and higher temperatures, the calculations are not very sensitive to temperature, making it impossible to extract reliable upper limits based on individual cases. Some of the transitions, e.g., the F_γ's for ^{7}Be(0.43→g.s.), ^{8}Li(0.98→g.s.), ^{13}C(3.09-3.85→g.s.), ^{16}O(6.13→g.s.), ^{15}N(5.27+5.30→g.s.), ^{15}N(7.16+7.57→5.27), and the ratio $R_\gamma = F_{\gamma 1}/F_{\gamma 2}$ for ^{11}C(6.34-7.50→g.s./4.32→g.s.), deviate from the overall trends, with the calculations and data in disagreement by more than 20% for T≈3-4 MeV. Such discrepancies could be due to incomplete information about specific spectroscopic data, which strongly influence the calculations for these nuclei. Or they could indicate non-thermal excited state populations, either in these or heavier nuclei, which feed these transitions by sequential decay processes. To illustrate the modifications due to feeding from particle unbound states, the dashed lines show the results of calculations which include feeding from higher-lying particle-stable states, but not from particle-unstable states.

To provide a more quantitative comparison between calculations and experimental data, we have performed a least squares analysis, computing the function,

$$\chi^2_\nu = \frac{1}{\nu} \cdot \sum_i^\nu \frac{(y_{exp,i} - y_{cal,i})^2}{\sigma_i^2} \qquad (1)$$

where $y_{exp,i}$ and $y_{cal,i}$ are the ith experimental and calculated values of the γ-ray fraction, F_γ is the ratio of γ-ray fractions, R_γ; ν is the number of independent data points (ν=28 for F_γ's, and ν=12 for R_γ's); and $\sigma_i^2 = \sigma_{exp,i}^2 + \sigma_{cal,i}^2$ is an uncertainty associated with the comparison for the ith measured quantity. In the latter expression, $\sigma_{exp,i}$ is the experimental uncertainty; $\sigma_{cal,i}$ reflects the range of calculated values corresponding to the different assumptions for the spins, isospins and parities of low-lying states where this information is incomplete. $\sigma_{cal,i}^2$ was computed as the variance of the calculations shown, for example, in Fig. 2.

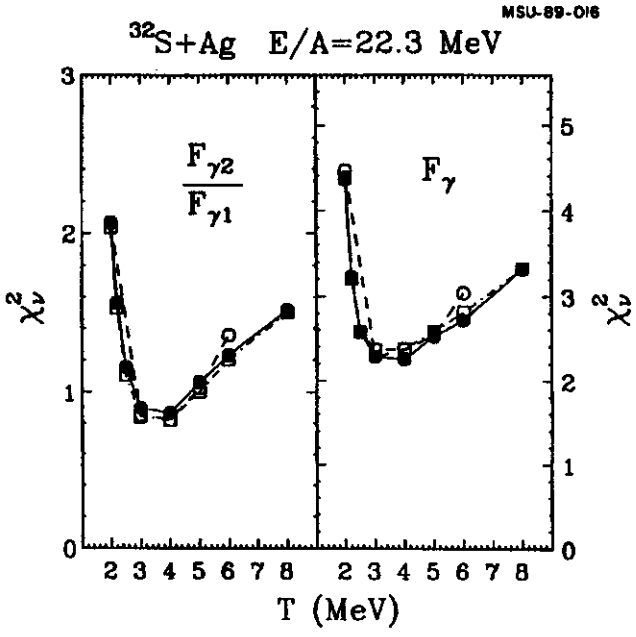

FIG. 3: The results of the least-squares analysis, χ^2_ν, for the ratios of γ-ray fractions, R_γ, and γ-ray fractions, F_γ, are shown in the left- and right-panels, respectively. Details are discussed in the text.

Values of χ^2_ν calculated for R_γ's and F_γ's are shown in the left and right windows of Fig. 3, respectively. The solid and open circles depict the values of χ^2_ν obtained for excitation energy cutoffs of μ = 3 and 5 MeV, respectively, when the unknown spectroscopic information for low-lying discrete states are chosen according to the noninteracting shell model. For comparison, the open squares show the results calculated for an excitation energy cutoff of μ = 3 MeV, when the unknown spectroscopic information for low-lying discrete states are chosen according to a much simpler scheme, in which:

1. Spins of 0-4 (1/2-9/2) are assumed with equal probability for even A (odd A) nuclei,
2. Isospins are assumed to be the same as the corresponding ground state isospin, and

3. Parities are assumed to be odd or even with equal probability. For all calculations, minimum values for χ^2_ν are observed in the region of $T \approx$ 3 to 4 MeV for both sets of measurements.

In summary, we have investigated a large number of particle-stable states of intermediate mass fragments for ^{32}S-induced reaction on Ag at E/A=22.3 MeV. Most of transitions are consistent with emission temperatures of $T \approx$3 to 4 MeV. This result is significant, since it describes a large number of measured values in terms of a single parameter. This, ultimately, must be the experimental justification of statistical treatments.

Fifteen percent of the transitions disagree with current calculations at T≈3 to 4 MeV. This could be due to incomplete spectroscopic information about certain decay channels which were important to these transitions, or it could indicate non-thermal contributions populated either in these nuclei or in heavier nuclei which could sequentially feed these states.

References

a. Present address: Nuclear Chemistry Division, Lawrence Livermore National Laboratory, Livermore, CA 94550

b. Department of Chemistry, Washington University, St. Louis, MO 63130

c. Physics Division, Oak Ridge National Laboratory, Oak Ridge, TN 37830

1. J. Pochodzalla *et al.*, Phys. Lett. 161B, 275 (1985).
2. D.J. Morrissey *et al.*, Phys. Rev. C34, 761 (1986).
3. C.B. Chitwood *et al.*, Phys. Lett. 172B, 27 (1986).
4. H.M. Xu *et al.*, Phys. Lett. 182B, 155 (1986).
5. L.G. Sobotka *et al.*, Phys. Rev. C34, 917 (1987).
6. J. Gomez del Campo *et al.*, Phys. Rev. Lett. 61, 290 (1988).
7. J. Pochodzalla *et al.*, Phys. Rev. C35, 1695 (1987).
8. Z. Chen *et al.*, Nucl. Phys. A473, 564 (1987).
9. C. Bloch *et al.*, Phys. Rev. C36, 203 (1987).
10. A. Galonsky *et al.*, Phys. Lett. B197, 511 (1987).
11. Z. Chen *et al.*, Phys. Rev. C36, 2297 (1987).
12. H.M. Xu *et al.*, Phys. Rev. C 40, 186 (1989).
13. M. Jaaskelainen *et al.*, Nucl. Instrum. Methods 204, 385 (1983).
14. F. Ajzenberg-Selove, Nucl. Phys. A392, 1 (1983); A413, 1 (1984); A433, 1 (1985); A449, 1 (1986); A460, 1 (1986).
15. Z. Chen and C.K. Gelbke, Phys. Rev. C38, 2630 (1988).
16. W. Hauser and H. Feshbach, Phys. Rev. 87, 366 (1952).
17. B.A. Brown, private communication.

Fragmentation Products With Nonstatistical Excited-State Populations

T.K. Nayak, T. Murakami, W.G. Lynch, K. Swartz,[a] D.J. Fields,[b] C.K. Gelbke, Y.D. Kim, J. Pochodzalla,[c] M.B. Tsang, H.M. Xu, F. Zhu, and K. Kwiatkowski[d]

Intermediate mass fragment emission is an important decay mode of highly excited nuclear systems.[1,2] Different fragmentation models reach different conclusions about the information provided by this process; for certain models intermediate mass fragment emission could even provide information about adiabatic instabilities, which lead to the liquid-gas phase separation of highly excited nuclear matter.

Both microscopic and statistical models of intermediate mass fragment emission can reproduce selected observables, like the fragment mass distribution. These models differ significantly, however, with respect to assumptions concerning the densities, internal excitation and degree of thermalization that prevail while the system proceeds from breakup to thermal freezeout. Statistical models frequently assume that the intrinsic degrees of freedom of the emitted fragments are fully thermalized and the asymptotic excited states of these fragments are populated statistically, with weights determined by the excitation energy or "temperature" of the emitting system.

This freezeout assumption can be tested by investigating whether the population probabilities of a large number of states in a single fragment follow predicted statistical distributions. In such a test, we have measured populations of particle-unstable states of ^{10}B nuclei. These measured populations differ significantly from those predicted by statistical models.

In the experiment, ^{14}N ions of 35 MeV/nucleon from the K500 cyclotron were bombarded on a natural silver target of about 0.5 mg/cm^2 thickness. Isotopically resolved light particles ($Z \leq 2$) and intermediate-mass fragments ($Z \geq 3$) were detected by a close-packed tetragonal array of 13 position-sensitive telescopes.[3] Nine telescopes, each having a solid angle of 4.5 msr and consisting of an *x-y* position-sensitive proportional counter, a 200-μm silicon-surface barrier detector, a 5-mm lithium-drift silicon detector, and a 10-cm-thick NaI(Tl) detector, were used to detect light particles. The four remaining telescopes, each having a solid angle of 5.7 msr and consisting of an *x-y* position-sensitive proportional counter, two planar surface-barrier detectors, 75 and 100μm thick, and a 5-mm lithium-drift silicon detector, were used to detect of intermediate mass fragments.

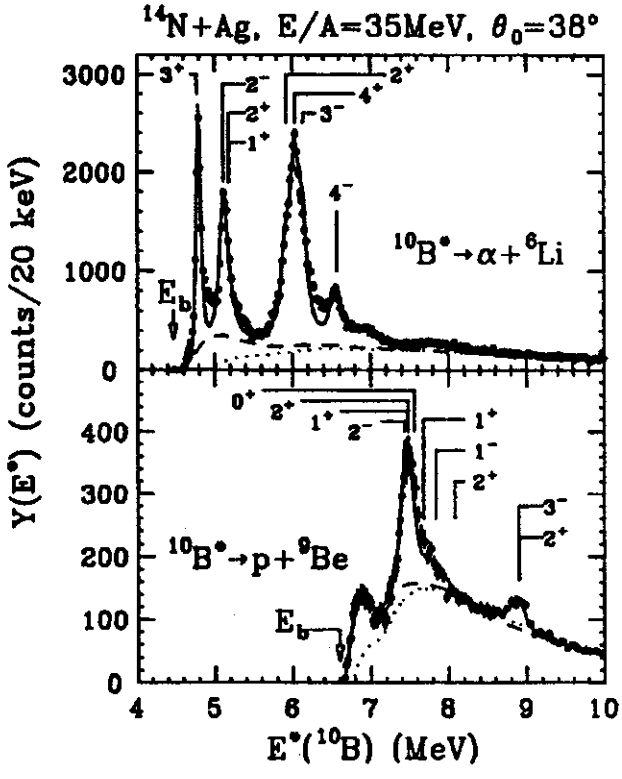

FIG. 1: The measured coincidence yields, Y(E*), as functions of excitation energy in ^{10}B. Arrows indicate the separation energy E_b for each decay channel.

Relative populations of particle-unstable states in ^{10}B nuclei were measured by detecting the coincident decay products for the channels $^{10}B^* \rightarrow {}^{9}Be + p$ and $^{10}B^* \rightarrow {}^{6}Li + \alpha$. Figure 1 shows the measured coincidence yields, *Y(E*)*, as functions of excitation energy in ^{10}B. Arrows indicate the separation energy E_b for each decay channel. A number of distinct peaks can be seen in the coincidence yields corresponding to particle-unstable excited states of ^{10}B nuclei. The location and spins of the relevant states are indicated

in the figure. The coincidence yields consists of a contribution, Y_c, from the decay of particle-unstable ^{10}B nuclei and a background, Y_b, for processes which do not proceed through the decay of excited ^{10}B nuclei. The background cross section is parametrized and is shown by the dashed lines in Fig. 1. An alternate assumption for the background, used for the estimate of systematic errors, is shown by the dotted lines.

The yield $Y_c(E^*)$ is related to the energy spectrum $|\, dn(E)/dE \,|$ for decay into channel c by the equation

$$Y_c(E^*) = \int \epsilon_c(E^*, E) \left| \frac{dn(E)}{dE} \right|_c dE,$$

where $\epsilon_c(E^*,E)$ is the efficiency function for the response of the hodoscope to the decay products of the particle unstable nuclei; E^* and E denote the measured and actual excitation energies, respectively. The excitation-energy spectrum for channel c can be written as

$$\left| \frac{dn(E)}{dE} \right|_c = \sum_i n_i \frac{(2J_i+1)\Gamma_i/2\pi}{(E-E_i)^2 + \Gamma_i^2/4} \left(\frac{\Gamma_{c,i}}{\Gamma_i} \right)$$

where n_i, E_i, J_i and $\Gamma_{c,i}/\Gamma_i$ are the relative population, centroid, spin, and branching ratio for the ith particle, respectively. The fits to the coincidence yields are shown by the solid curves in Fig. 1.

In Fig. 2 the solid points with error bars give the final relative populations for the different groups of states as functions of excitation energy. If the intrinsic degrees of freedom of the system are thermalized at low density, the initial populations of the excited states of intermediate-mass fragments should be proportional to the Boltzmann factor $\exp(-E^*/T)$. The measured relative populations deviate significantly from this monotonic behavior.

Detailed calculations were performed to obtain these ratios, assuming a thermal distribution of primary fragments and taking sequential feeding from higher-lying states into account. These calculations include the experimentally known discrete states, as well as continuum states up to an excitation energy E^*/A = 5 MeV, where A is the mass of the fragment. The open boxes in the figure give the range of values from such calculations for a 4 MeV initial temperature, where the uncertainties due to unknown spin and

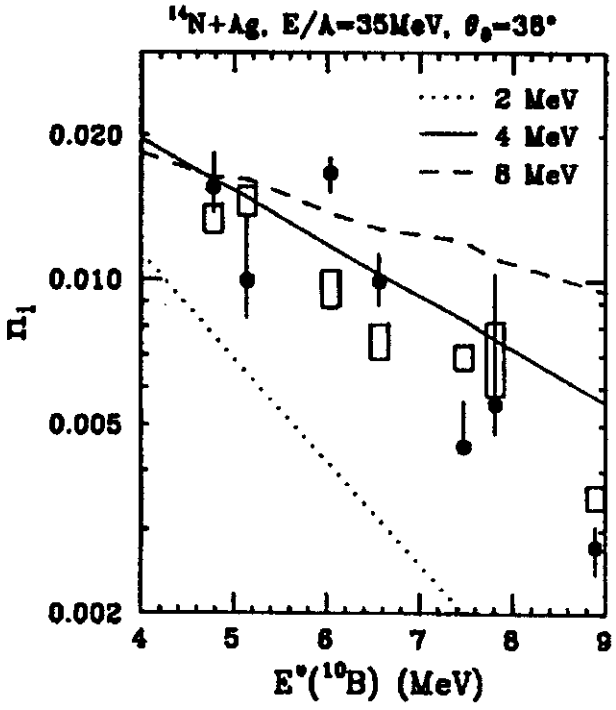

FIG. 2: Relative populations, n_i, of different groups of particle-unstable states in ^{10}B plotted as functions of excitation energy. The vertical scale is normalized so that $\sum_k (2J_k+1)n_k = 1$, where the summation is restricted to the particle-stable states of ^{10}B.

parities are included. Clearly, the calculation does not reproduce the measured ratios at 6.0 MeV, 6.56 MeV, 7.46 MeV and 8.9 MeV. Starting with a different initial temperature does not significantly improve the agreement.

This inconsistency of the statistical assumption with the experimental observables suggests that the asymptotic excited states of isolated fragments may not be statistically populated in these reactions.[4]

References

a. Nuclear Physics Laboratory, University of Washington, Seattle, WA 98195.

b. Physics Division, Lawrence Livermore National Laboratory, Livermore, CA 94550.

c. Institut für Kerphysik, Universität Frankfurt, D-6000 Frankfurt, Federal Republic of Germany.

d. Department of Chemistry and Physics and Indiana University Cyclotron Facility, Indiana University, Bloomington, IN 47405.

1. "Proceedings of the Symposium on Central Collisions and Fragmentation Processes," edited by C.K. Gelbke, Nucl. Phys. A471C, 1-451 (1987).

2. W.G. Lynch, Ann. Rev. Nucl. Part. Sci. 37, 493 (1987).

3. T. Murakami *et al.*, Nucl. Instrum. Method Phys. Res. Sect. A275, 112 (1989).

4. T.K. Nayak *et al.*, Phys. Rev. Lett. 62, 1021 (1989).

Multifragment Emission Processes

N. Carlin, R. DeSouza, C.K. Gelbke, W.G. Gong, Y.D. Kim, W.G. Lynch, T. Nayak, M.B. Tsang, H.M. Xu, F. Zhu, L. Sobotka[a], and D.G. Sarantites[a]

Multifragment disintegrations of highly excited nuclear systems formed in violent nuclear reactions are of considerable interest, since such processes might contain key information concerning the liquid-gas phase diagram of nuclear matter.[1-4] Experimental information on such processes is still very limited. While multifragment emission of intermediate mass fragments (IMF: $3 \leq Z \leq 20$) has been clearly identified[5-7] for nucleus-nucleus collisions at higher energies ($E \geq 3$ GeV) the extent of this process has not yet been clearly established at energies available at the NSCL. At these lower energies, the IMF angular distributions are strongly forward-peaked,[8,9] indicating emission on time scales shorter than the rotational period of the composite system.[9] Thus, most fragments are produced in fast processes, even though fragment emission at backward angles, $\Theta_{c.m.} \geq 120°$, may be attributed to the statistical, but not necessarily sequential[10] decay of equilibrated reaction residues.[11-14]

While some multifragment decay processes have been observed,[8,15,16] it has been argued recently that fast IMF emission is simply a form of binary deep inelastic scattering.[17] To investigate this issue, we used a large solid-angle charged-particle detection system,[18] to measure the IMF multiplicity distributions for fragments emitted behind the grazing angle in ^{36}Ar-induced reactions on ^{238}U at E/A = 35 MeV. In order to discriminate between central, fusion-like collisions and less violent peripheral collisions, the IMF multiplicity distributions were measured in coincidence with two fission fragments from the decay of the associated heavy reaction residues.

In this experiment, performed at the K500 cyclotron, charged particles were detected with 96 phoswich detectors of the "Dwarf-Ball-Wall" array developed at Washington University.[18] Each phoswich detector consisted of a thin fast-plastic scintillator foil followed by a thick CsI(Tl) scintillator, with 200-μm plastic scintillation foils and 20-mm CsI(Tl) scintillators at the forward angles, reducing to 40-μm foils and 4-mm CsI(Tl) scintillators at the backward angles. To suppress secondary electrons and X-rays, the Dwarf-Ball detectors (located at $\Theta \leq 35°$) and Dwarf-Wall detectors (located at $12° \leq \Theta \leq 35°$) were covered by 5-mg/cm^2-thick Au foils and 10-mg/cm^2-thick Ta foils, respectively.

The most forward detectors at $\Theta \leq 12°$, covering the grazing angle, were shielded by 1-mm Pb absorbers to stop elastically scattered projectiles. These absorbers also stopped IMF's, but allowed the detection of energetic light particles. For light particles, the detection array provided an angular coverage corresponding to about 85% of 4π. For heavy fragments, the coverage was reduced to about 78% of 4π. About 1% of the loss in coverage was due to the Pb absorbers; additional angular coverage was lost because of poor elemental resolution for detectors located at $\Theta \leq 150°$.

Particle identification was achieved by integrating the photomultiplier anode current over three different time gates. This information was combined to obtain the energy of the detected particle, as well as elemental identification up to about $Z = 6$, and isotopic identification for light particles ($Z \leq 2$). Light particles not stopped in the CsI scintillators could still be identified elementally. Fission fragments were detected with two *X-Y*-position-sensitive parallel-plate multiwire detectors covering angular ranges of $\Theta_1 = 36°$-$116°$, and $\Theta_2 = -(39°$-$89°)$ in the reaction plane. In the off-line analysis, energy thresholds of 12 and 18 MeV for hydrogen and helium nuclei, respectively, were used for the Dwarf-Ball detectors. For the Dwarf-Wall detectors, the thresholds were 20 MeV for both hydrogen and helium. All heavier particles which passed through the absorber and scintillator foils were analyzed; the resulting fragment energy thresholds were E/A≈6 to 9 MeV and E/A≈2 to 3 MeV for the Dwarf-Wall and Dwarf-Ball detectors, respectively.

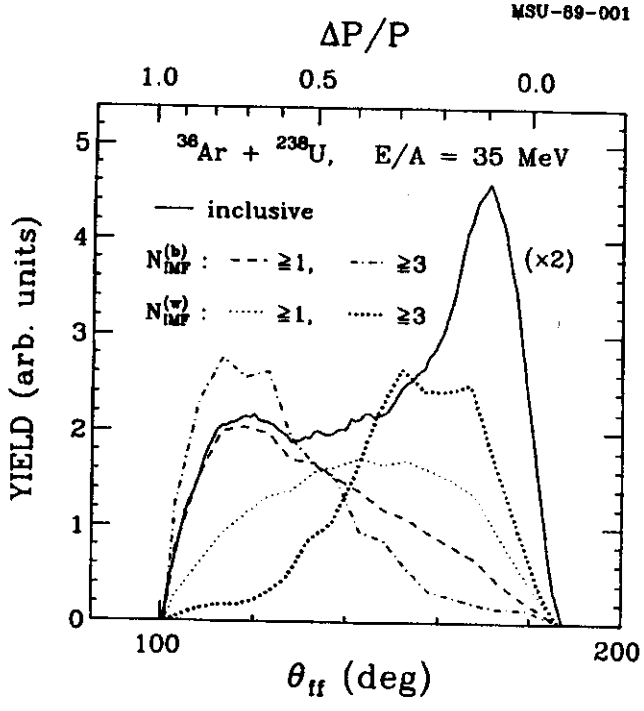

FIG. 1: Folding angle distributions between coincident fission fragments. The various gating conditions are explained in the text. For convenience of comparison, the distributions are normalized to identical integral yields; the inclusive distribution has been multiplied by a factor of 2.0.

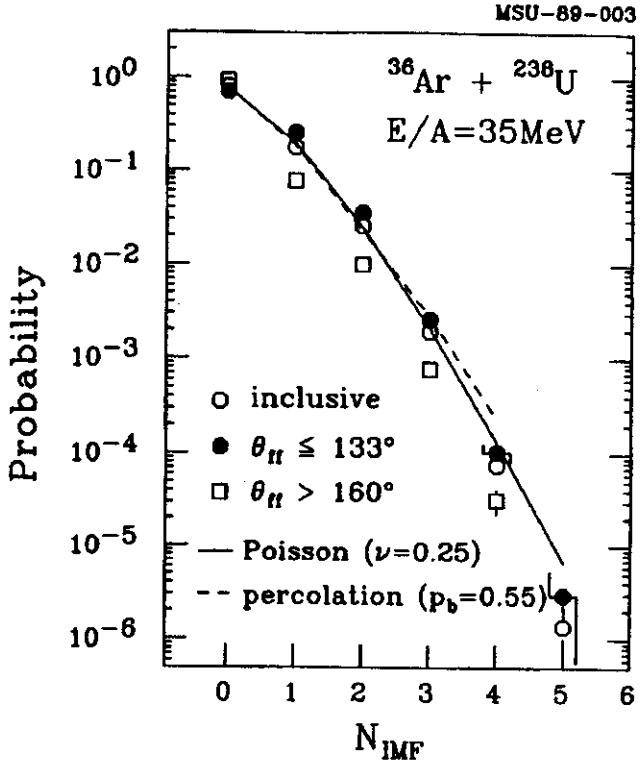

FIG. 2: Number of single- and multi-fragment emission processes detected per fission trigger. Open circles: no gate on Θ_{ff}; open squares: $\Theta_{ff} > 160°$; solid points: $\Theta_{ff} < 133°$. Solid curves represent Poisson distributions, $P(N,\nu) = e^{-\nu}\nu^N/N!$; dashed curves are predictions of a percolation model.[20]

Figure 1 shows distributions of folding angles between coincident fission fragments, $\Theta_{ff} = \Theta_{f1} + \Theta_{f2}$. For orientation, the upper scale of the figure gives the linear momentum transfer, $\Delta P/P$, to the heavy reaction residue in units of the projectile momentum, P, assuming symmetric fission of the compound nucleus. The solid line shows the inclusive distribution for fission-fission coincidences. The dashed and dotted-dashed curves show distributions gated by the detection of at least one and three intermediate mass fragments in the Dwarf-Ball, $N^{(b)}_{IMF} \geq 1$ and 3, respectively. The emission of intermediate mass fragments to larger angles can be associated with violent, fusion-like collisions characterized by large linear momentum transfers.[13] The folding angle distributions gated by $N^{(b)}_{IMF} \geq 1$ and 3 are remarkably similar, indicating that single and multi-fragment emissions to intermediate and large angles ($\Theta \geq 35°$) correspond to similar classes of reactions. The light and heavy dotted curves show distributions gated by the detection of at least one and three intermediate mass fragments in the Dwarf-Wall, $N^{(w)}_{IMF} \geq 1$ and 3, respectively. The condition $N^{(w)}_{IMF} \geq 1$ does not select a very specific class of collisions; there are contributions from incomplete fusion reactions as well as from peripheral collisions. On the other hand, the requirement $N^{(w)}_{IMF} \geq 3$ places a bias towards more peripheral collisions with smaller linear momentum transfers to the heavy reaction residue.

Figure 2 shows probabilities for observed multiplicities, N_{IMF}, of intermediate mass fragments for different gates on folding angle. These observed multiplicities represent the number of detected particles; they can be smaller than the actual multiplicities of emitted particles due to finite detection thresholds and incomplete solid angle coverage. Open circles correspond to "inclusive" fission-fission triggers, with no gate placed on folding angle; open squares correspond to small momentum transfer collisions gated by $\Theta_{ff} > 166°$ ($\Delta P/P < 0.2$); solid points correspond to large momentum transfer collisions gated by $\Theta_{ff} \leq 133°$ ($\Delta P/P \geq 0.5$). The occurrence of multifragment emission processes is clearly established. Fragment emission occurs

with significantly higher probabilities in central collisions characterized by large linear momentum transfers. The observed multiplicity distributions decrease monotonically and are rather well described by Poisson probability distributions (shown by solid curves). No special role is played by events with $N_{IMF}=1$ since they are otherwise indistinguishable from events with higher multiplicities. Since intermediate mass fragment emission is, in general, associated with non-negligible light particle multiplicities and could therefore occur through multifragmentation processes, it does not clarify matters to classify events with $N_{IMF}=1$ as "binary" events.[10]

Poisson distributions are characteristic of processes which occur with a low and constant probability. Such conditions may prevail for nuclear decays at high excitation energies and with low fragment multiplicities. For example, the statistical weight for fragment emission is small compared to that for light particle emission, when calculated in a statistical rate equation approach, such as a sequential evaporation model.[12,19] In this case, deviations from Poisson distributions would be expected to occur mainly for high fragment multiplicities or small systems when emission probabilities are affected by energy or mass conservation. Detailed calculations are required to assess which models can reproduce the measured multiplicity distributions. To illustrate that Poisson distributions may also be expected in a static theory which encompasses a phase transition, we show in Fig. 2 distributions predicted by the percolation model[20] for the percolation parameters, p, indicated in the figure. (Because of distortions from detection thresholds and incomplete solid angle coverage, our data cannot provide a definitive value for the percolation parameter, p, or the expectation value, ν, of the Poisson distribution; a more quantitative analysis is beyond the scope of the present measurement.)

To further test the assumption of statistically independent emissions, with a reduced sensitivity to the detection inefficiency, we have examined the "charge-correlation function",

$$C(Z_1,Z_2)=N_0\frac{\sum_{i\neq k}Y_{ik}(Z_1,Z_2)}{\sum_{i\neq k}Y_i(Z_1)\cdot Y_k(Z_2)} \quad (1)$$

Here, $Y_{ik}(Z_1,Z_2)$ denotes the coincidence yield for particles of charge number Z_1 and Z_2 detected in detectors i and k, respectively, and $Y_i(Z)$ denotes the singles yield for particles of charge number Z in detector i. To eliminate peripheral interactions, fission fragment folding angles were restricted to $\Theta_{ff}\leq 133°$ and at least one intermediate mass fragment, designated by index i, was required to be detected in the Dwarf-Ball ($\Theta \geq 35°$). The summation over k includes all detectors in the Dwarf-Ball-Wall array. The measured values are listed in Table I. They are constant within about $\pm 10\%$, supporting the concept of nearly independent statistical emissions.

TABLE I: Charge-correlation function defined in Eq. 1 of the text. To simplify comparisons, the correlation function was normalized to one for $Z_1=Z_2=5$.

$Z_1\downarrow \ \backslash \ Z_2\Rightarrow$	Li	Be	B	C
Li	1.05	0.92	0.97	0.94
Be	1.13	1.01	1.04	1.00
B	1.06	0.91	1.00	0.91
C	1.10	1.01	1.01	0.93

The definitive observation of multifragment emission processes for the $^{36}Ar+^{238}U$ reaction at E/A = 35 MeV is stimulating. Even though multifragment observables depend on impact parameter, the single and multiple emissions of intermediate mass fragments to large angles ($\Theta \geq 35°$) occur essentially in reactions characterized by large associated charged particle multiplicities and large linear momentum transfers to the heavy reaction residues. The measured fragment multiplicity distributions are well described by Poisson distributions, and the measured charge correlation functions are constant within about $\pm 10\%$. Both observations are consistent with a stochastic emission process. Final states with only one intermediate mass fragment in the exit channel represent only one of a family of final states.

References

a. Washington University

1. J.E. Finn *et al.*, Phys. Rev. Lett. 49, 1321 (1982).

2. R.J. Lenk *et al.*, Phys. Rev. C34, 177 (1986).

3. X. Campi, J. Phys. G19, L917 (1986); Phys. Lett. B208, 351 (1988).

4. J.A. Lopez *et al.*, Nucl. Phys. A431, 728 (1984).

5. J.W. Harris *et al.*, Nucl. Phys. A471, 241c (1987).

6. K.G.R. Doss *et al.*, Phys. Rev. Lett. 59, 2720 (1987).

7. R. Bougault *et al.*, Nucl. Phys. A488, 255c (1988).

8. D.J. Fields *et al.*, Phys. Rev. C34, 536 (1986).

9. D.E. Fields *et al.*, Indiana University preprint (1988).

10. D.H.E. Gross, Phys. Lett. B203, 26 (1988).

11. L.G. Sobotka *et al.*, Phys. Rev. Lett. 51, 2187 (1983).

12. W.A. Friedman *et al.*, Phys. Rev. C28, 950 (1983).

13. M. Fatyga *et al.*, Phys. Rev. Lett. 58, 2527 (1987).

14. D. Bowman *et al.*, Phys. Lett. B189, 282 (1987).

15. D. Pelte *et al.*, Nucl. Phys. A488, 251c (1988).

17. B. Borderie *et al.*, Phys. Lett. B205, 26 (1988).

18. D.G. Sarantites *et al.*, Nucl. Instrum. Methods A264, 319 (1988). The fast-slow plastic phoswich elements of the original device were replaced by plastic-CsI(Tl) phoswich elements.

19. J. Gomez del Campo *et al.*, Phys. Rev. Lett. 61, 290 (1988).

20. W. Bauer *et al.*, Nucl. Phys. A452, 699 (1986).

Extended Emission Sources Observed Via Two-Proton Correlations

T.C. Awes[a], R.L. Ferguson[a], F.E. Obenshain[a], F. Plasil[a], G.R. Young[a], S. Pratt[b], Z. Chen, C.K. Gelbke, W.G. Lynch, J. Pochodzalla[c], and H.M. Xu

Two-particle correlations between light particles emitted in heavy-ion reactions have been used to extract information for the formation and decay of localized regions of high excitation.[1-5] In this report, we present an analysis of the directional dependence of the two-particle correlation function and extract the shape of the proton emission source.[6]

The experiment was performed at the Holifield Heavy-Ion Research Facility in Oak Ridge. A natural Ag target of 9.9-mg/cm^2 areal density was bombarded by a ^{32}S beam of 22.3-MeV/nucleon incident energy. Protons were detected by a close-packed hexagonal array of 13 ΔE-E telescopes. Each telescope consisted of a 400-μm-thick Si detector and a 10-cm-thick NaI detector, and each subtended a solid angle of 0.67 msr with an angular separation of 4.1° between adjacent telescopes. The hodoscope was centered at a laboratory angle of 30°. An energy threshold of 12 MeV has been used in the off-line analysis.

The correlation function R(**K**,**q**) is extracted from the ratio of the coincidence yield, $Y_{12}(\mathbf{p}_1,\mathbf{p}_2)$, to the singles yields, $Y_1(\mathbf{p}_1)$ and $Y_2(\mathbf{p}_2)$, of particles 1 and 2, according to:

$$\sum Y_{12}(\mathbf{p}_1,\mathbf{p}_2) = C_{12}[1 + R(\mathbf{K},\mathbf{q})]\sum Y_1(\mathbf{p}_1)Y_2(\mathbf{p}_2), \quad (1)$$

where $\mathbf{p}_1$ and $\mathbf{p}_2$ are the momenta of the two protons and **K** and **q** are the total and relative momenta of the pair, respectively. The single overall normalization constant, C_{12}, was chosen such that after summing Eq. (1) over all |**K**| and directions, R(|**q**|) averages to zero in the interval $52 \le |\mathbf{q}| \le 80$ MeV/c. For each gating condition, the sums on both sides of Eq. (1) were extended over all detector and proton-energy combinations corresponding to the given bins of **q**.

Theoretical values for the correlation function may be calculated as[7]

$$1 + R(\mathbf{K},\mathbf{q}) = \frac{\int d^3r F_K(\mathbf{r})\phi(\mathbf{q},\mathbf{r})}{\int d^3r F_K(\mathbf{r})} \quad (2)$$

with

$$F_K(\mathbf{r}) = \lim_{t\to\infty} \int d^3R f\left(\frac{\mathbf{K}}{2}, \mathbf{R}+\frac{\mathbf{r}}{2}, t\right) f\left(\frac{\mathbf{K}}{2}, \mathbf{R}-\frac{\mathbf{r}}{2}, t\right)$$

where φ is the correctly antisymmetrized wave function of relative motion for the two correlated protons. $F_K(\mathbf{r})$ is the relative Wigner function, and $f(\mathbf{K}/z, \mathbf{R}, t)$ is the single particle Wigner function for any time after many-body interactions have ceased.[7]

The lifetime cannot be determined uniquely from the correlation function, as there is only spatial dependence in Eq. (2). However, a long source lifetime will stretch the relative Wigner function $F_K(\mathbf{r})$ along the direction of the particle velocity.[7] Evaporative models predict long lifetimes, and therefore yield distinctive prolate emission sources for protons emitted with energy near the Coulomb barrier. Protons of higher energy escape more quickly, yielding less-elongated source shapes.

Figure 1 shows the measured directional dependence of the correlation function for the ^{32}S+Ag reaction, for gates on the total kinetic energy of the emitted proton pair of E_{pp}=60-70 and 90-100 MeV. For each energy gate, the correlation function is shown for relative momenta, either parallel (Θ=0°±30°, or Θ=180°±30°) or transverse (Θ=90°±30°) to the direction of the emitted proton pair. Within statistics, no difference was observed between transverse directions in and out of the reaction plane; therefore, all transverse directions have been summed together.

The finite size of the detector hodoscope introduced cutoffs in the relative momentum, which are clearly seen in Fig. 1. For relative momenta in the longitudinal direction,

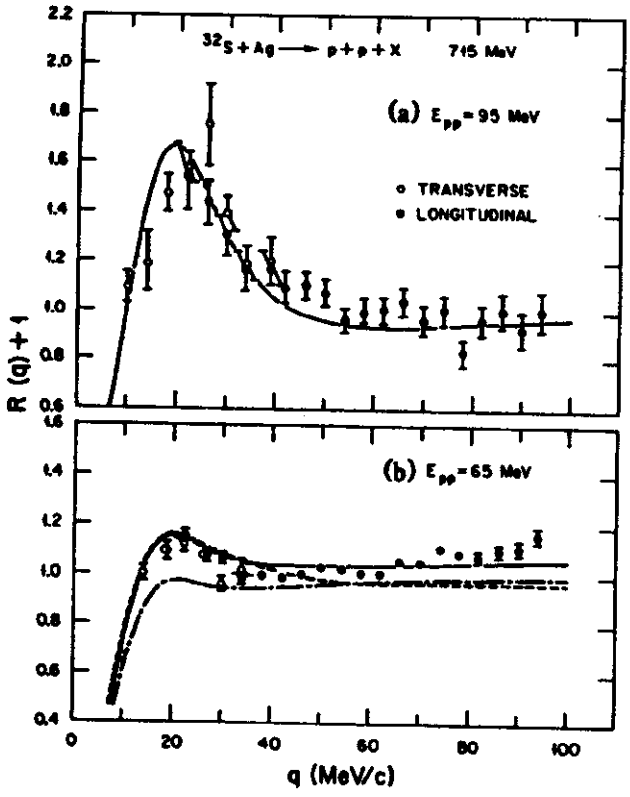

FIG. 1: Proton-proton correlations for the ^{32}S + Ag reaction at 715-MeV incident energy. The correlation is shown for relative momenta in the longitudinal (solid circles) and transverse (open circles) directions, relative to the direction of the total momentum of the proton pair. The correlations are shown for total laboratory kinetic energy for the proton pair, for (a) $90 < E_{pp} < 100$ MeV together with the calculated correlation for $R_T = R_L = 4$ fm, and (b) $60 < E_{pp} < 70$ MeV together with calculations for $R_T = R_L = 6.5$ fm (solid line) and $R_T = 4$ fm, $R_T = 20$ fm. (Longitudinal correlation = dashed line; transverse correlation = dot-dashed line). The normalizations of the two calculations of (b) are not the same. Errors reflect the statistical uncertainty only.

the minimum angle between adjacent detectors introduces a cutoff at small q. Similarly, the maximum angle between detectors introduces a cutoff at large q for relative momenta transverse to the direction of emission. The location of these cutoffs has been verified by a Monte Carlo calculation, which included the geometrical acceptance and energy and angular resolution of the hodoscope.

Also shown in Fig. 1 are theoretical curves obtained by our evaluating Eq. (2) for nonspherical Gaussian-shaped sources of longitudinal and transverse "radii" R_L and R_T as follows:

$$F_K(r, t \to \infty) = F_0 \exp - \left(\frac{x^2 + y^2}{R_T^2} + \frac{z^2}{R_L^2} \right) \qquad (3)$$

The wave functions ϕ were found by solving Schrödinger's equation with the Reid soft-core potential for the $l=0,1$ partial waves and with only the Coulomb potential for the higher waves. The theoretical correlation functions were averaged over the same directions as the experimental bins. Since the theoretical calculation does not include the dynamics necessary to predict the absolute probability of two-particle-to-one-particle events, the theoretical curves were multiplied by a different factor for each energy gate to match the experimental correlation function.

At high proton-emission energies, both the longitudinal and transverse correlations are observed to exhibit strong enhancements of approximately equal strength [see Fig. 1(a)]. The similarity of the correlation in the two directions indicates a spherical emission source. The calculation shown in Fig. 1(a) corresponds to the correlation expected from a spherical source of negligible lifetime and compound-nucleus dimensions of $R_L = R_T = 4$ fm. More surprising is the result seen in Fig. 1(b) that, although the correlation is weaker for low proton-emission energies, no obvious directional dependence is observed. The weak angle-integrated correlations observed for low-energy protons have previously been suggested to results from extended emission times, as from the later stages of an evaporative process. Calculated correlations are shown for an evaporative-type source with a transverse radius of 4 fm and a longitudinal dimension of 20 fm. Although the calculated longitudinal correlation is in reasonable agreement with the experimental result, the theoretical transverse correlation is suppressed, as a result of the short transverse dimension, in contrast to the observed result. It is seen that a better description of the low-energy proton results is obtained by the assumption of a spherical source of about 6.5-fm radius.

The sensitivity of the observed longitudinal and transverse correlations to the emission shape is illustrated in Fig. 2. In this example, the transverse dimension of the source has been fixed at that of compound system (4 fm) and the calculated values of the longitudinal and transverse correlations at q=25 (where the two correlation differ strongly) are shown for increasing longitudinal source size,

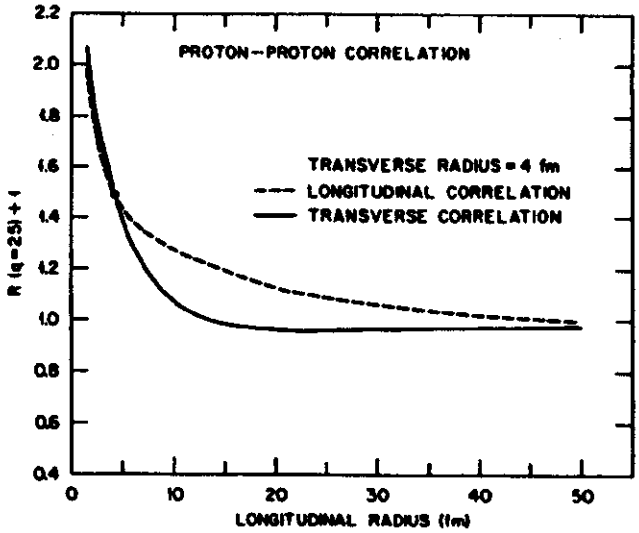

FIG. 2: Longitudinal-radius dependence of the longitudinal and transverse proton-proton correlations at a relative momentum of 25 MeV/c for a source with a transverse radius of 4 fm.

or equivalently, increasing lifetime. As shown, in the figure, the difference between the longitudinal and transverse correlations is small when the two dimensions are similar or when the longitudinal dimension becomes very large. However, for very large longitudinal radii, that is, for long lifetimes, the correlation itself becomes very weak because of the increased volume, contrary to the observation [see Fig. 1(b)].

The energy dependence of the proton emission-source shape is shown in more detail in Fig. 3, for proton-pair total kinetic energies ranging from 105 to 55 MeV. The source radii were extracted by fitting the measured longitudinal and transverse correlations to the theoretical correlations obtained with Eqs. (2) and (3). As noted in the discussion of Fig. 1, although the high- energy protons appear to be emitted on a short time scale from a volume consistent with the combined system, the low-energy protons appear to be emitted from an extended spherical volume of up to twice the compound-nucleus, rather than being emitted over a extended period of time from the compound nucleus. The trend expected for the case of evaporative compound-nucleus emission is also indicated in Fig. 3. In this case, the transverse radius would remain equal to the compound-nucleus radius (R_T=4 fm), while the longitudinal radius will appear to increase by the emission lifetime τ, $R_L = (R_T^2 + V_K^2\tau^2)^{1/2}$. It should be pointed out that the lowest proton energies considered here are still considerably above the Coulomb barrier,where a long evaporation time scale would clearly be expected. However, because of the experimental uncertainties and the weakness of the observed correlation at the lowest proton-pair kinetic energy of 55 MeV, the loose upper bound on the longitudinal radius does not exclude the possibility that the emission source may, in fact, be elongated because of the emission time scale; the large transverse radius does, however, require a large spatial extent (see Fig. 3).

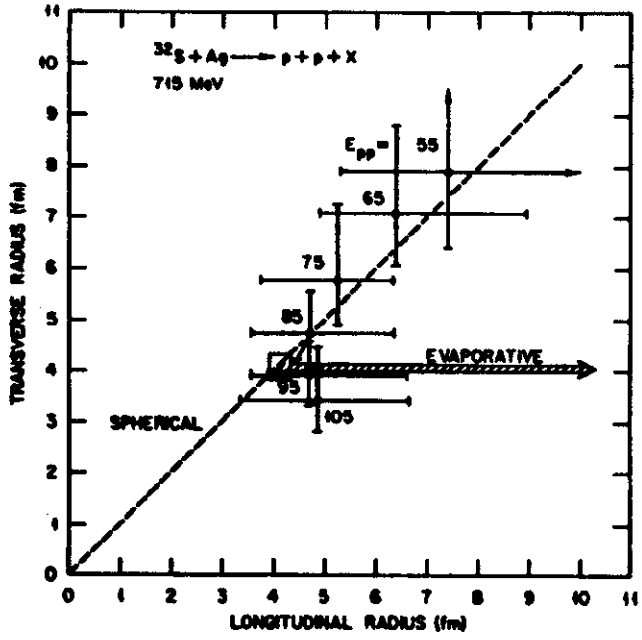

FIG. 3: Longitudinal and transverse radii obtained by our fitting the calculated correlations to the experimental longitudinal and transverse two-proton correlations for the ^{32}S + Ag reaction at 715 MeV. Results are shown for proton-pair kinetic energies ranging from 55 to 105 MeV. The error bars are conservative estimates obtained by independent variations which double the X^2, which varied from 1.2 to 5.6. At 55 MeV the upper bounds on the radii are essentially open. The equivalent sharp sphere radii are $\sqrt{5/2}$ larger than the indicated radii if the rms radii are equated (see the discussion of Fig. 1 in the text).

In conclusion, the observed directional dependence of the proton-proton corrections suggests that the lower-energy protons may be emitted from an extended source which has expanded to be considerably larger than the compound system rather than from the compound system over an extended period of time.

References

a. Oak Ridge National Laboratory, Oak Ridge, Tennessee 37831.

b. Department of Physics, University of Wisconsin, Madison, WI 53706.

c. Institut fur Kernphysik, Johan-Wolfgang-Goethe Universität, 6000 Frankfurt, Federal Republic of Germany.

1. W.G. Lynch *et al.*, Phys. Rev. Lett. 51, 1850 (1983).

2. C.B. Chitwood *et al.*, Phys. Lett. B 172, 27 (1986).

3. J. Pochodzalla *et al.*, Phys. Lett. B 174, 36 (1986).

4. J. Pochodzalla *et al.*, Phys. Rev. C35, 1695 (1987).

5. Z. Chen *et al.*, Nucl. Phys. A473, 564 (1987).

6. T.C. Awes *et al.*, Phys. Rev. Lett. 61, 2665 (1988).

7. Scott Pratt and M.B. Tsang, Phys. Rev. C36, 2390 (1987).

Entropy Production in Heavy-Ion Collisions

W.K. Wilson, D. Cebra, J. Clayton, C. Djalali, D. Fox, S. Howden, J. Kam, A. Nadasen, C.A. Ogilvie, A. Pradhan, A. Vander Molen, J. Van der Plicht, G. Westfall, and J. Winfield

Introduction

A major research goal in heavy-ion reaction physics is the study of nuclear matter under extreme conditions of temperature and pressure. In order to draw conclusions about the properties of hot nuclei, observables should be chosen which are sensitive to the early processes of the reaction and unchanged by the later expansion and cooling. Theoretical models[1,2] suggest that entropy production is a potentially rewarding observable since it saturates in the initial hot, compressed stage of the collision.

We are completing a systematic study of entropy production in heavy-ion collisions with beam energies ranging from 20 to 800 MeV/nucleon. Results of our inclusive measurements of entropy production performed with the Bevalac accelerator at Berkeley using Ar beams from 42 to 137 MeV/nucleon on Au have been published previously. This report will present results of both inclusive and exclusive measurements performed with the K500 cyclotron at NSCL using beams from 20 to 35 MeV/nucleon Ar incident on Au and V targets. We conclude that entropy production increases with beam energy.

Entropy production is not a direct observable and can only be measured by comparing experimental data with a model. This is typically done by comparing fragment production cross sections with the predictions of the Quantum Statistical Model (QSM).[3,4,5] This model assumes that thermal and chemical equilibrium is established within some subset of the nucleons participating in the reaction. One must detect the fragments produced from this subset, then vary the entropy and breakup density parameters in the QSM until a best fit to the cross sections is obtained.

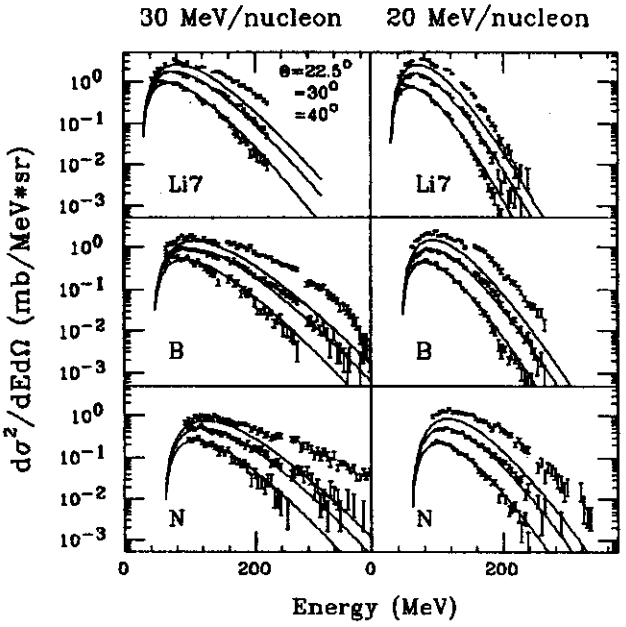

FIG. 1: Representative sample of kinetic energy spectra obtained in Ar+Au reactions. The fits are from a moving Maxwell-Boltzman source.

Inclusive Studies

Measurements of intermediate mass fragment (IMF) cross sections ($3 \leq Z \leq 12$) were performed with beams of 20 and 30 MeV/nucleon Ar, incident on a Au target. Figure 1 displays a representative sample of kinetic energy spectra taken at three angles with Si stack detectors operating in minimum-bias trigger mode. We achieved mass resolution for Li and Be, and charge resolution up to Mg. The energy-and-angle-integrated cross sections were extracted by fitting a moving Maxwell-Boltzman source to the 30° and 40° spectra. This procedure isolated the participant source as the equilibrated subset for comparison with the QSM. The backward angles are fit better than the most forward angles, since the latter have contributions from projectile fragmentation.

The standard χ^2 function was used to find the best fit to the production cross sections. As an example, Fig. 2 shows the χ^2 surface as a function of the temperature and breakup

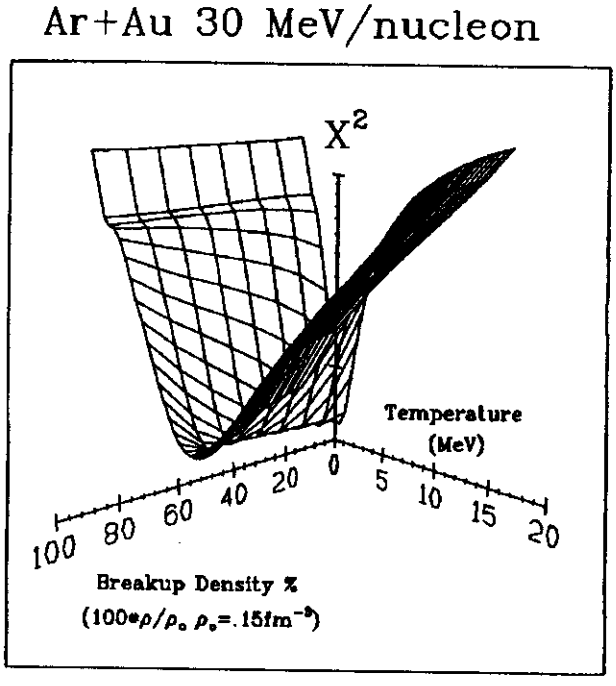

FIG. 2: χ^2 minimization as a function of the temperature and breakup-density QSM parameters.

density QSM parameters for the 30 MeV/nucleon data. There is a pronounced minimum in χ^2 as a function of temperature but no such minimum appears as a function of density. Given the size, temperature, and density of the system, the QSM calculates the entropy of the system, so the uncertainty in breakup density leads to a corresponding uncertainty in entropy.

The results of our fits are shown in Fig. 3 with preliminary error bars. Taken along with the Bevalac data for the same system, the entropy is clearly seen to decrease with decreasing beam energy.

Also shown in Fig. 3 is a theoretical curve based on complete thermalization of the projectile's incident energy.[5] The data cannot be compared directly to the curve, since the theory was calculated for infinite nuclear matter and is thus expected to underestimate the entropy production. However, the decreasing disparity between the data and theory at low beam energies does suggest that thermalization is becoming a relatively more important channel for energy dissipation as the beam energy decreases.

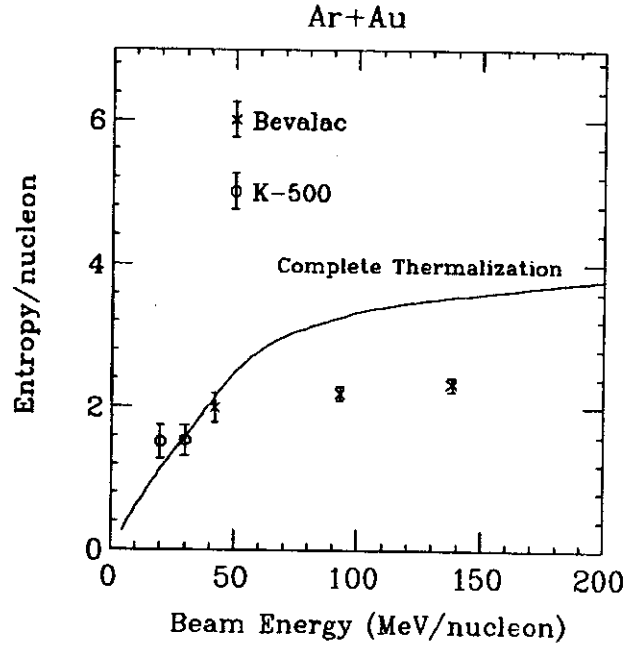

FIG. 3: Entropy production in Ar+Au reactions as a function of beam energy.

Exclusive Studies

One potential criticism of the inclusive measurements is the possible error introduced by averaging impact parameters, and the difficulty of evaluating the error. Experiments performed by the Plastic Ball Group at Berkeley show a strong impact parameter dependence in the entropy extracted from light particle production ($Z \leq 2$).[5] In order to evaluate the influence of averaging at lower beam energies, experiments have been performed with 35 MeV/nucleon Ar beams on Au and V targets using the MSU 4π array. For these experiments, the 4π array consisted of 215 phoswich detectors covering 85% of 4π sr. Total charge collected within a rapidity window midway between projectile and target rapidity was used as an measure of the centrality of the event.[6]

The light particle production as a function of mid-rapidity-charge is shown in Fig. 4 as a ratio to protons. In Fig. 5, a similar plot is shown for IMF ratios, again as a function of mid-rapidity-charge. Light particle production was found to depend weakly on impact parameter, while heavier fragments were observed to be preferentially emitted from central collisions.

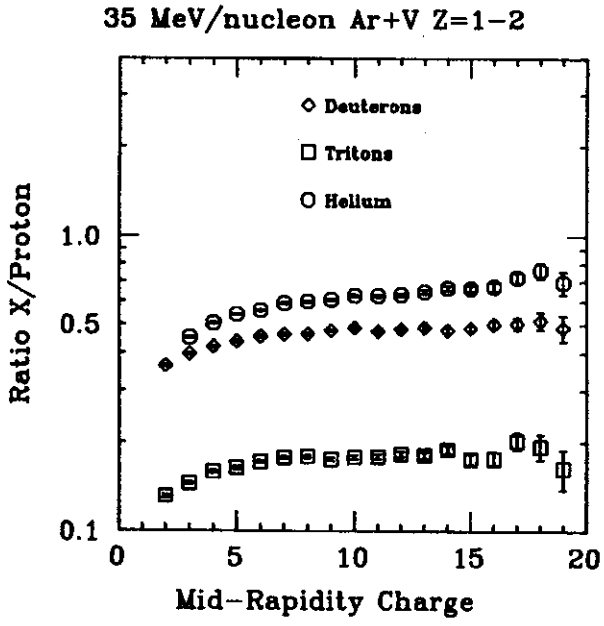

FIG. 4: Light particle production as a function of mid-rapidity-charge. (MSU 4π)

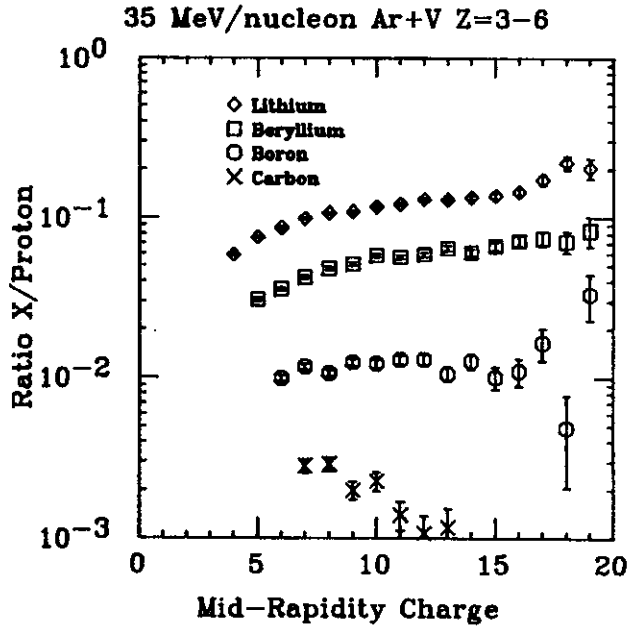

FIG. 5: Intermediate mass fragments as a function of mid-rapidity-charge. (MSU 4π)

We are currently evaluating the effects of our detector acceptance on observed fragment cross sections.

References

1. J.I. Kapusta and D. Strottman, Phys. Rev. C23, 2514 (1981).
2. G. Bertsch and J. Cugnon, Phys. Rev. C24, 2514 (1981).
3. B.V. Jacak *et al.*, Phys. Rev. Lett. 51, 1946 (1983).
4. D. Hahn and H. Stöcker, Nucl. Phys. A476, 718 (1988).
5. K.G.R. Doss *et al.*, Phys. Rev. C37, 163 (1988).
6. C.A. Ogilvie *et al.*, (to be published).

Triple Differential Cross Sections from 35 MeV/n Ar + V

D.A. Cebra, J. Clayton, S. Howden, J. Karn, A. Nadasen, C.A. Ogilvie, A. Vander Molen, G.D. Westfall, W.K. Wilson, and J. Winfield

The MSU 4π array allows the researcher to study fragment cross-sections as a function of energy, polar angle (Θ), azimuthal angle (Φ), and impact parameter *(b)*. Using the information available in these multiparticle measurements, one can better characterize the sources of the fragments produced in the reaction.

One would expect the source velocities, temperatures, and sizes which are fit to the data to vary as a function of the centrality of the collision. Peripheral interactions will produce distributions which are dominated by fragments originating from the cold target and projectile remnants, while for central events, a large intermediate velocity thermal source will produce most of the observed fragments.[1]

One can also compare the relative importance of collective versus thermal effects. Collective effects may show a strong memory of the reaction plane, defined by the vector connecting the centers of the target and the projectile and the vector along the beam axis, while thermal effects should be isotropic in the rest frame of the interaction region.

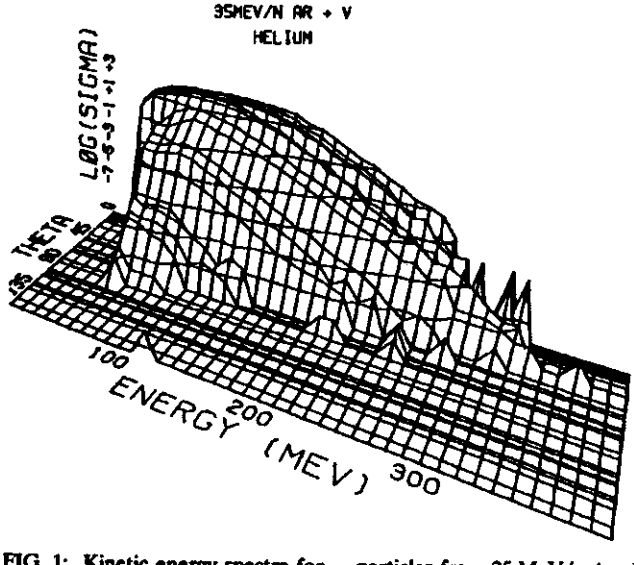

FIG. 1: Kinetic energy spectra for α particles from 35 MeV/n Ar+V emitted in reaction plane (Φ = 0±22.5°).

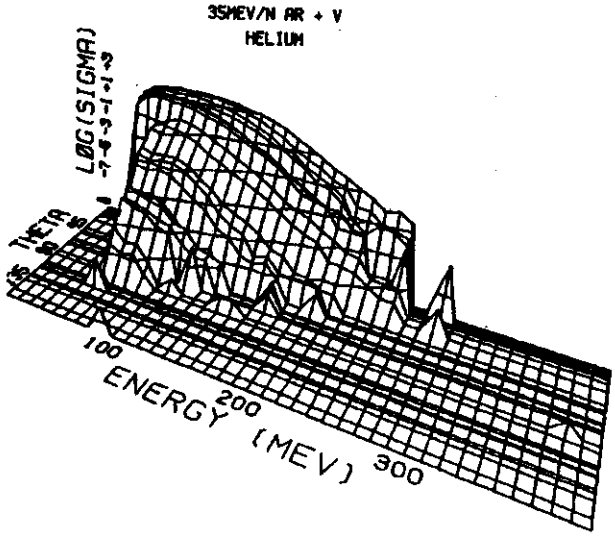

FIG. 2: Kinetic energy spectra for α particles from 35 MeV/n Ar+V emitted out of the reaction plane (Φ = 90±22.5°).

Figure 1 displays the triple differential cross-sections as a function of energy and polar angle for helium fragments emitted in the reaction plane (Φ = 0±22.5°) from the reaction $^{40}Ar+^{51}V$ at 35 MeV/n. Figure 2 shows the spectra for helium fragments emitted perpendicular to the reaction plane (Φ = 90±22.5°). The height axis labeled LOG(SIGMA) is the log of the cross section

$$\frac{d^3\sigma}{dEd(\cos\Theta)d\Phi}$$

The spacing of the curves as a function of Θ is not uniform because each curve represents a specific set of detectors, the central angles (Θ, Φ) of which are defined by the position in the 4π array. The low-energy cut-offs for the cross sections at a given angle is defined by the thickness of the ΔE scintillators (1.5 mm thick for the forward array [Θ ≤ 20°] and 3.175 mm thick for the standard 4π modules [Θ ≥ 20°]). The observed angular distributions for several particle types, impact parameters, and azimuthal angles

have been reproduced assuming a moving thermal source. Adjustable parameters considered are: σ (size of the source), τ (temperature), and β (velocity of the fit source).

TABLE I: Moving source parameters for α particles from 35 MeV/n Ar+V.

b (b_{max})	σ (mb)	β (c)	τ (MeV)
0.0-0.1	12	.094	13.17
0.1-0.4	181	.114	11.83
0.4-0.9	1874	.131	11.81
0.9-1.0	810	.207	5.61

TABLE II: Moving source parameters for α particles from 50 MeV/n C+C.

b (b_{max})	σ (mb)	β (c)	τ (MeV)
0.0-0.2	8	.062	9.48
0.2-0.5	113	.150	7.99
0.5-1.0	432	.231	5.15

The results of the study of fragment cross sections as a function of impact parameter *(b)* are presented in Table I. The impact parameter was determined on an event-by-event basis using the intermediate rapidity charge.[2] One observes that σ, source size, increases with increasing b. This is a simple geometric effect; the σ should increase as $\int b\,db$. β, the "fit" source velocity, increases from 40% beam velocity for central collisions (V_{cm} = 44% V_{beam}), to 75% for the most peripheral. τ, temperature, varies inversely with b. Data from 50 MeV/n ^{12}C + ^{12}C are presented in Table II. The results of this analysis are similar.

Figures 3 and 4 show the σ and τ parameters from the moving source "fits" for protons, heliums, and lithiums, as a function of Φ. In order to determine Φ for each fragment, it is necessary to estimate the reaction plane for every event. We construct a vector Q defined as

$$Q = \Sigma_i^n p_i^t \omega_i$$

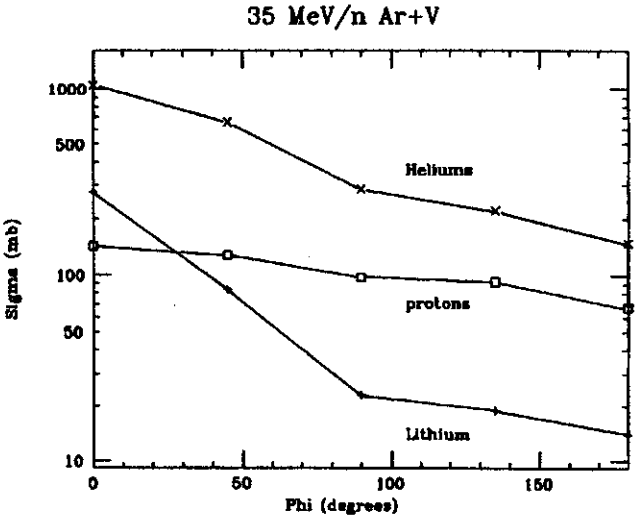

FIG. 3: Extracted σ parameters (cross sections) as a function of azimuthal angle.

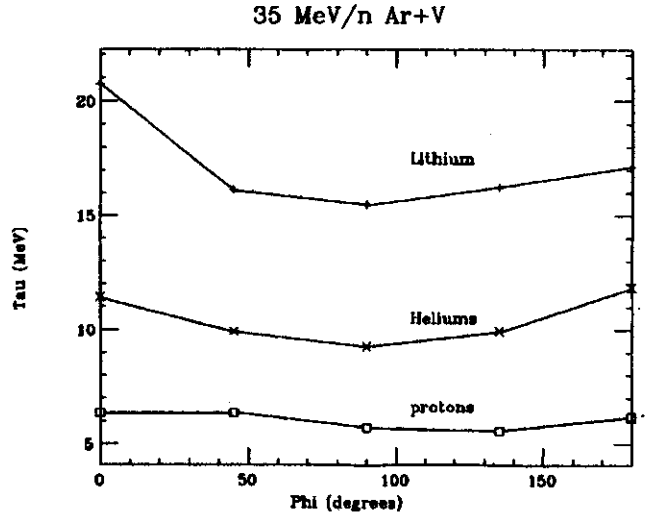

FIG. 4: Extracted τ parameters (temperatures) as a function of azimuthal angle.

where p_i^t is the momentum vector transverse to the beam direction and ω_i is a weighting factor, which is equal to $\pm m_i$, depending on whether the fragment was emitted forward or backwards in the center-of-mass frame. This vector has been shown to agree with the known reaction plane to within $\pm 20°$ for simulated events.[3] The extracted cross sections drop exponentially with increasing Φ, indicating a strong in-plane enhancement. τ, or temperature, drops for out-of-plane data. This suggests that within the reaction plane, particles have some collective motion in addition to the thermal kinetic energy. This collective

motion could be a rotation of the interaction region. The kinetic energy of particles emitted in or near the reaction plane would thus be enhanced, and one would extract an overestimate of τ. By comparing the apparent temperature shifts in- and out-of-plane, one can measure the relative importance of the thermal and the collective motion.

We have studied the kinetic energy spectra as a function of impact parameter and azimuthal angle. One concludes that the simple fireball model must be expanded to include collective effects in order to explain all of the observed features of this data set. Clearly the angular momentum must be included.

References

1. G. Westfall *et al.*, Phys. Rev. Lett. 37, 1202 (1976).
2. C. Ogilvie *et al.*, Phys. Rev. C, (to be published).
3. C. Ogilvie *et al.*, (to be published).

Transverse Collective Motion in Intermediate-Energy Heavy-Ion Collisions

C.A. Ogilvie, D.A Cebra, J. Clayton, P. Danielewicz, S. Howden, J. Karn,
A. Nadasen[a], A. Vander Molen, G.D. Westfall, W.K. Wilson and J.S. Winfield

The study of collective motion[1-3] produced in heavy-ion collisions has contributed to our understanding of the reaction dynamics involved in these complicated processes. The collective motion is often extracted by the global transverse momentum analysis introduced by Danielewicz and Odyniec.[4] This probes the presence of directed collective motion in the reaction plane and provides a quantitative measure of the transverse component of this collective motion, against which detailed microscopic models (Vlasov-Uehling-Uhlenbeck[5] and Quantum Molecular Dynamics[6]) can be compared.

Several years ago, Molitoris *et al.*[7] predicted that at low bombarding energies the directed transverse momentum would correspond to negative-angle scattering caused by mean-field effects. This is in contrast to the behavior at higher beam energies (E>200 MeV/nucleon), where the collective motion is understood to correspond to positive-angle scattering due to hydrodynamical side-splash effects. Unfortunately, the global transverse momentum analysis cannot determine the overall sign of the directed momentum. However, by examining a range of results from different beam energies, we may be able to infer from the magnitude of the data some evidence for a change of the reaction mechanism.

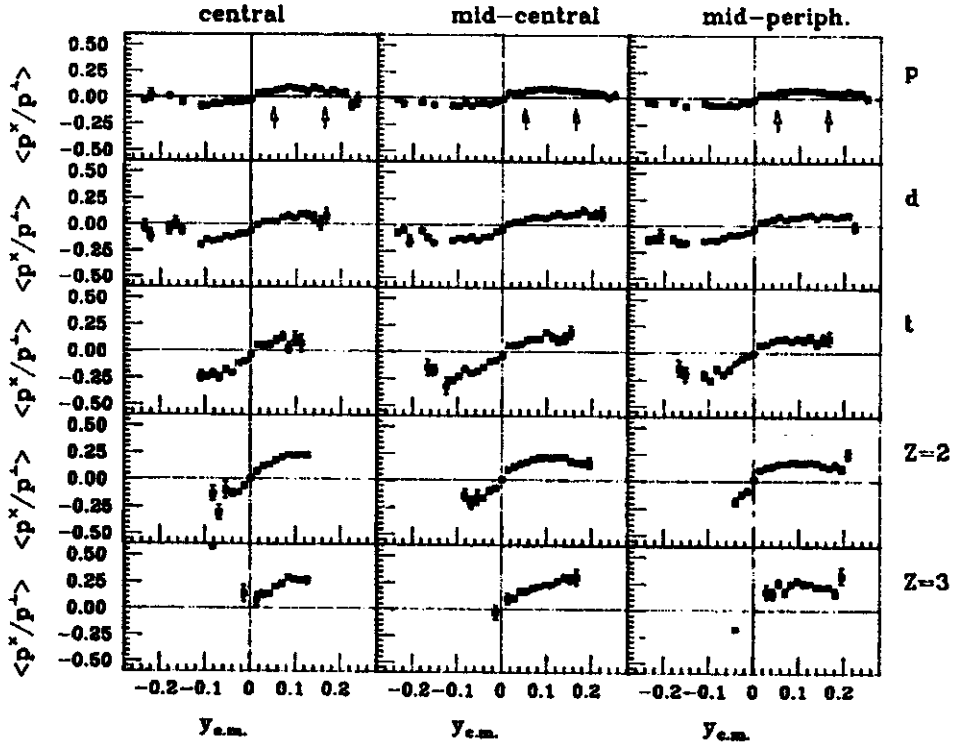

FIG. 1: The in-plane fraction of transverse momentum as a function of center-of-mass rapidity for fragments emitted in C+C collisions at 50 MeV/nucleon. The columns correspond to central, mid-central and mid-peripheral collisions respectively. The rows correspond to protons, deuterons, tritons, Z=2 and Z=3 fragments. The arrows correspond to the rapidity ranges used to calculate average quantities.

We have measured light charged fragments from the $^{12}C+^{12}C$ reaction at 50 MeV/nucleon and the $^{40}Ar+^{51}V$ reaction at 35 MeV/nucleon with Phase I of the MSU 4π array.[8] The beams were provided by the K500 cyclotron of the National Superconducting Cyclotron Laboratory. The Phase I configuration of the 4π array contains phoswiches only. Full details of the energy thresholds and angular coverage for this experiment are given in Ref. 9.

The data presented here have been filtered on an event-by-event basis into three impact parameter groups: central, mid-central and mid-peripheral collisions.[10] These groups have been gated by the mid-rapidity charge (Z_{mr}) where Z_{mr} is the sum of the charges of those fragments that fall within the rapidity window

$$0.75y_{targ} \leq y \leq 0.75y_{proj}$$

and y is the fragment's rapidity in the center-of-mass frame of the nuclei. The determination of the reaction plane is improved by requiring events to have at least three fragments above the energy thresholds, one of which must be in the backward center-of-mass hemisphere.

We have modified the standard analysis of transverse momentum by including a recoil correction. This accounts for momentum correlations due to momentum conservation and is important when the multiplicity is small and the collective effects are weak. Figure 1 shows the in-plane fraction of transverse momentum as a function of center-of-mass rapidity for protons, deuterons, tritons, He, and Li fragments emitted in central, mid-central and mid-peripheral C+C collisions at 50 MeV/nucleon. Transverse collective motion is observed for all fragment types. It is weakest for protons and increases in strength for the heavier fragments. The collective motion is similar for each of the impact parameter groups.

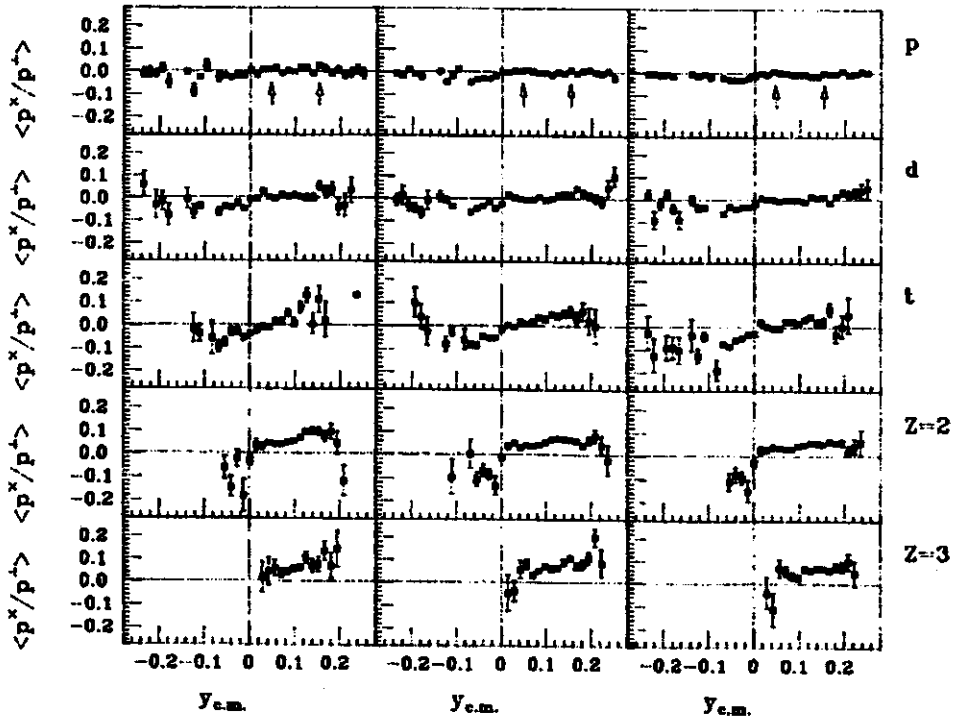

FIG. 2: As for Fig. 1 but for Ar+V collisions at 35 MeV/nucleon.

In Fig. 2 we plot the in-plane fraction of transverse momentum for Ar + V collisions at 35 MeV/nucleon. There is no statistically significant collective motion observed for the protons, and even for the deuterons the signal is very weak. Collective motion is observed for tritons and is present to a greater extent for helium and lithium fragments. There is no significant evidence that the collective motion is different for the central collisions than for the other two impact parameter bins.

In Fig. 3 we plot the reduced quantities

$$\frac{\overline{<p^x/A>}}{p_{proj/A}}$$

for a variety of systems at different beam energies. The quantity

$$\overline{<p^x/A>}$$

is the average transverse momentum near beam rapidity[9], while the scaling factor[12], p_{proj}/A, is the momentum per nucleon of the projectile in the center-of-mass frame of the nuclei. Our data have been extracted from mid-central collisions, averaged over all fragment types detected and have been renormalized to account for the dispersion in finding the reaction plane.

The other data shown are from experiments performed by the Streamer Chamber and Plastic Ball groups.[1,2,4,11] There exist other data down to 200 MeV/nucleon[3]; however, the literature only provides the slope of the transverse momentum at zero rapidity (the 'flow'). From Fig. 3 it is apparent that our Ar + V data are consistent with the transverse motion observed at higher energies. The fact that the C + C data show stronger collective effects than the Ar + V data possibly indicates that the transverse momentum has a different projectile mass dependence than when observed at higher energies. It is clear that a more systematic study (different systems at several beam energies) is needed before we can ascertain whether a change of mechanism has occurred.

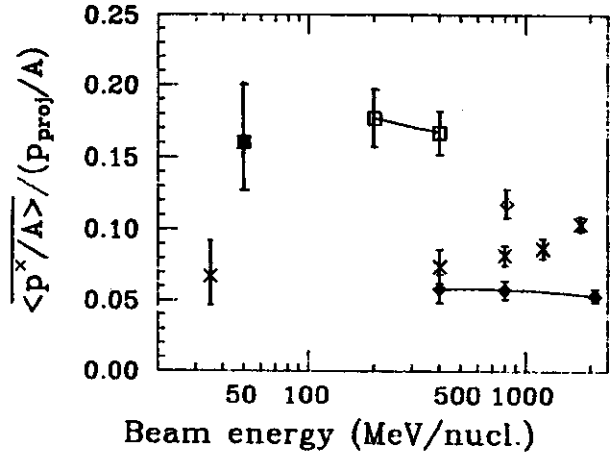

FIG. 3: The reduced transverse momentum per nucleon for a variety of systems over a range of bombarding energies. The two lowest energy points are our data in this paper; the solid square is from C + C, whereas the cross is from the Ar + V data. The crosses at higher energies are from Ar + KCL and Ca + Ca reactions performed by a GSI/LBL group.[1,4,11] The solid diamonds represent Ne + NaF collisions[2], the open squares Au + Au collisions[1], and the open diamonds La + La collisions.[11] The lines join the data for each symmetric system and are drawn to guide the eye.

References

a. University of Michigan, 4901 Evergreen Rd, Dearborn, MI 48128.

1. H.A. Gustafsson *et al.*, Mod. Phys. Lett. A3, 1323 (1988).

2. M. Vient, Ph.D. thesis, University of California, Riverside, 1988.

3. K.G.R. Doss *et al.*, Phys. Rev. Lett. 57, 302 (1986).

4. P. Danielewicz and G. Odyniec, Phys. Lett. B157, 146 (1985).

5. G.F. Bertsch and S. das Gupta, Phys. Reports 160, 189 (1988).

6. G. Peilart *et al.*, Phys. Rev. C39, 1402 (1989).

7. J.J. Molitoris, D. Hahn, and H. Stocker, Nucl. Phys. A447, 13c (1985).

8. G.D. Westfall *et al.*, Nucl. Instrum. Methods A238, 347 (1985).

9. C.A. Ogilvie *et al.*, (to be published).

10. C.A. Ogilvie *et al.*, Phys. Rev. C40, 654 (1989).

11. P. Danielewicz *et al.*, Phys. Rev. C38, 120 (1988).

12. A. Bonasera, L.P. Csernai and B. Schurmann, Nucl. Phys. A476, 159 (1988).

Determination of the Impact Vector in Intermediate-Energy Heavy-Ion Collisions

C.A. Ogilvie, D.A Cebra, J. Clayton, S. Howden, J. Karn,
A. Vander Molen, G.D. Westfall, W.K. Wilson and J.S. Winfield

To unravel the complex processes that occur during nuclear collisions, it is necessary to have a reaction mechanism filter; one that separates the central collisions from the grazing collisions, with some differentiation for the mid-impact collisions. Some quantities of interest also require a measurement of the direction of the impact vector. For example, the measurement of the collective flow produced in collisions[1] requires a determination of the reaction plane; i.e. the plane defined by the impact vector and the beam axis.

We have studied how well the impact vector can be determined experimentally in intermediate-energy heavy-ion collisions by simulating symmetric collisions of A=40 nuclei with the statistical event generator FREESCO.[2] The code uses a modified fireball prescription to generate four thermal sources, the size of which depend on the impact parameter. The four sources then de-excite via explosion and evaporation. The dynamics of this model may be somewhat inadequate at the bombarding energies considered here (E≤100 MeV/nucleon), but FREESCO's main advantage is that it provides the full range of possible fragments. Other models contain more detailed dynamics but can only produce nucleons or test-particles, e.g. the Vlasov-Uhling-Uhlenbeck model (VUU).[3] FREESCO provides an event-by-event simulation of the nuclear collisions, and from the final fragments we can construct several observables that are likely to depend on the impact parameter.[4]

We will discuss only two of these:

1) **Particle multiplicity:** As the impact parameter is reduced, more kinetic energy will be transferred to the internal energy of the colliding system. With high internal energy, the system is likely to disintegrate into more fragments. The physics of this disassembly is not fully understood, which means that the particle multiplicity is dependent on the fine details of the assumed model.

2) **Mid-rapidity-charge:** In symmetric collisions one expects the participant volume to increase with decreasing impact parameter. Integrating the charge of those particles that have rapidities y between $0.75 \times y_{c.m.}^{target}$ and $0.75 \times y_{c.m.}^{proj.}$ could provide a measure of the collision zone. Because of the integration, the mid-rapidity-charge is expected to be relatively insensitive to how the participant zone disassembles. This quantity is similar to the baryon charge multiplicity used in the Plastic Ball experiments.[5]

The angle of the impact vector, **b**, can be found using the method developed by Danielewicz and Odyniec.[6] Assuming there exists some collective transverse momentum in the reaction plane, then the vector **Q**:

$$\mathbf{Q} = \sum_{\nu=1}^{n} \omega_\nu \mathbf{p}_\nu^{\perp}$$

will lie in the reaction plane. The sum runs over all the fragments; ω_ν is a weighting factor that has an opposite sign for particles emitted in the forward and backward hemispheres in the center of mass, and $\mathbf{p}_\nu^{\perp}$ is the fragment's perpendicular momentum. We will compare how accurately **Q** reproduces the reaction plane.

Each of the impact parameter quantities and the direction of the impact vector were calculated for the full events as predicted by the simulation (both neutrons and charged particles). These events were then filtered by the response of the MSU 4π array[7] and the quantities recalculated.

Figure 1 displays the impact parameter dependence of the predicted multiplicity and the filtered multiplicity. Both the predicted and filtered multiplicity increase with bombarding energy and are monotonically dependent on the

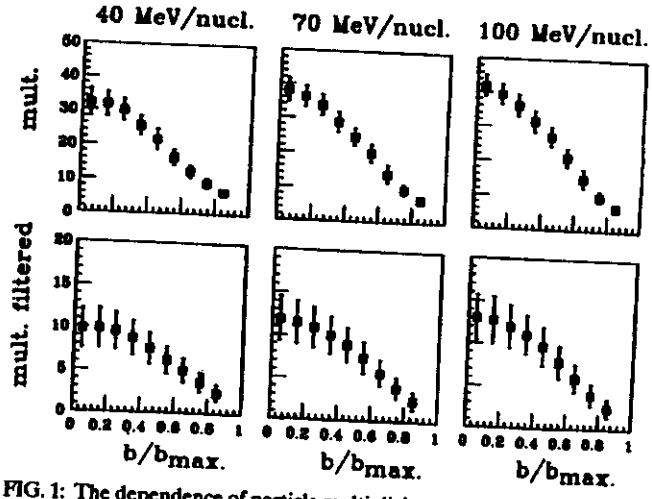

FIG. 1: The dependence of particle multiplicity on the impact parameter for $^{40}Ca+^{40}Ca$ at 40, 70, and 100 MeV/nucleon. The top and bottom panels correspond to the unfiltered and filtered results respectively. The data points represent the mean values and the error bars represent the one standard deviation width at each impact parameter.

impact parameter. This dependence flattens out for small impact parameters, especially for the lowest beam energy considered here.

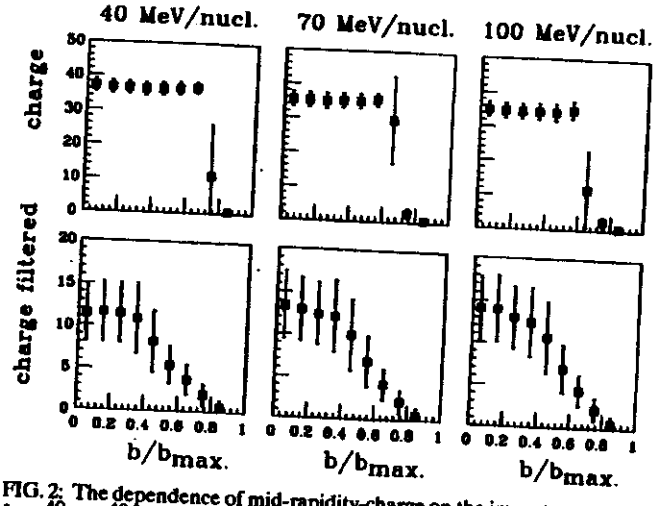

FIG. 2: The dependence of mid-rapidity-charge on the impact parameter for $^{40}Ca+^{40}Ca$ at 40, 70, and 100 MeV/nucleon.

The dependence of the mid-rapidity-charge resembles a step-function for the unfiltered data (Fig. 2). For collisions with $b < 0.7 \times b_{max}$, the projectile and target spectators lose sufficient center-of-mass kinetic energy to fall within the mid-rapidity window. The array's Z and E thresholds reduce the effect of these spectators, leaving a dependence on b that is likely to be caused by the changing size of the participant zone.

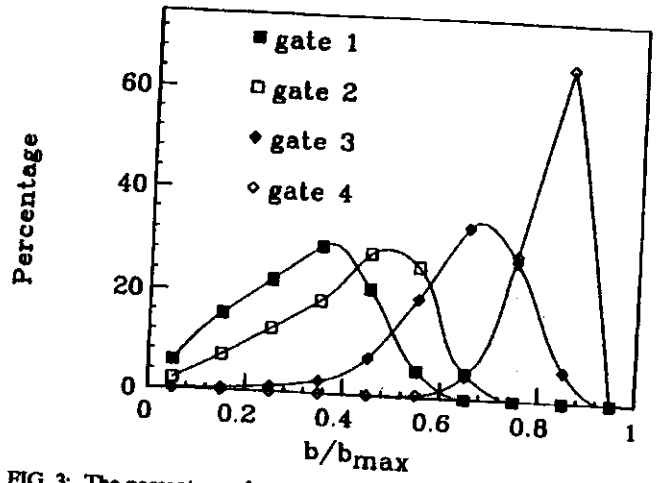

FIG. 3: The percentage of events within each mid-rapidity-charge gate that have a given impact parameter. The system is $^{40}Ca+^{40}Ca$ at 70 MeV/nucleon after filtering through the acceptance of a 4π detector. The lines through the points are to guide the eye and have been found by a three-point smoothing algorithm.

In the analysis of an experiment, gates that are placed on either the mid-rapidity-charge or the multiplicity will select out events that span a range of impact parameters. Typical gates for the filtered mid-rapidity-charge produce the sampled impact-parameter ranges shown in Fig. 3 for 70 MeV/nucleon. The behavior is similar for the other two energies. This figure shows the percentage of events within each gate that have a given impact parameter.

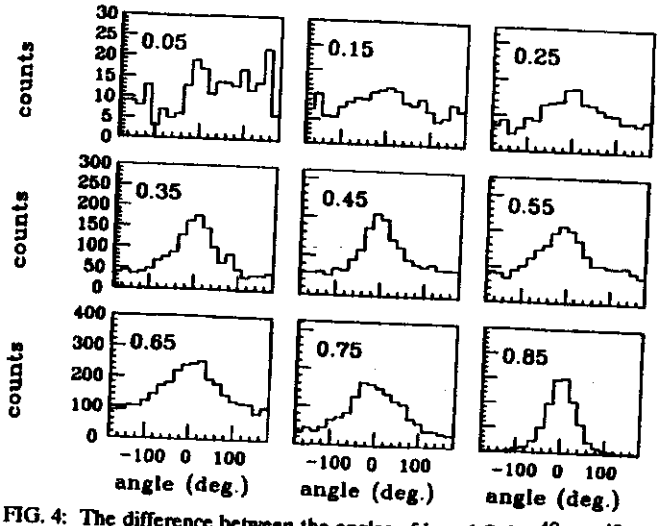

FIG. 4: The difference between the angles of b and Q for $^{40}Ca+^{40}Ca$ at 70 MeV/nucleon after filtering. The weights used for Q were $\omega_i = p_t^i$, and the impact parameter bin (b/b_{max}) is given in the upper left corner.

In FREESCO, the angle of the impact vector is known. Therefore, if Q accurately reproduces the reaction plane it will lie parallel to b. In Fig. 4 we plot the difference in angles

between Q and b after filtering through the 4π's acceptance. The distributions (for different impact parameters) each have a maximum at 0°. The widths of these distributions are not greater than a half width at half maximum of 70° for $b > 0.25 \times b_{max}$.

References

1. K.G.R. Doss *et al.*, Phys. Rev. Lett. 57, 302 (1986).
2. G. Fai and J. Randrup, Nucl. Phys. A 404, 551 (1983), and Comp. Phys. Comm. 42, 385 (1986).
3. G.F. Bertsch and S. Das Gupta, Phys. Report 160, 189 (1988).
4. C.A. Ogilvie *et al.*, Phys. Rev. C 40, 654 (1989).
5. K.G.R. Doss *et al.*, Phys. Rev. C 32, 116 (1985).
6. P. Danielewicz and G. Odyniec, Phys. Lett. 157B, 146 (1985).
7. G.D Westfall *et al.*, Nucl. Instrum. Methods A238, 347 (1985).

Study of a Transverse Momentum Excitation Function at Intermediate Energies

D. Krofcheck, G.M. Crawley, C. Djalali[a], S. Howden, C.A. Ogilvie, A. Vander Molen, G.D. Westfall, W.K. Wilson, and R.S. Tickle[b]

The reaction dynamics for heavy-ion collisions in the energy range of ($20 \leq E_{lab} \leq 200$) MeV/nucleon are sensitive to the nuclear mean field as well as to individual nucleon-nucleon interactions. It has been proposed[1] that the transition between a repulsive reaction mechanism at the higher energies[2], to an attractive mean field mechanism at the lower energies[3], may be manifested in the transverse momentum spectrum. Indeed, the average transverse momentum is predicted to go through zero at the lower energies, indicating a switch from positive to negative scattering angles as the reaction mechanism changes.

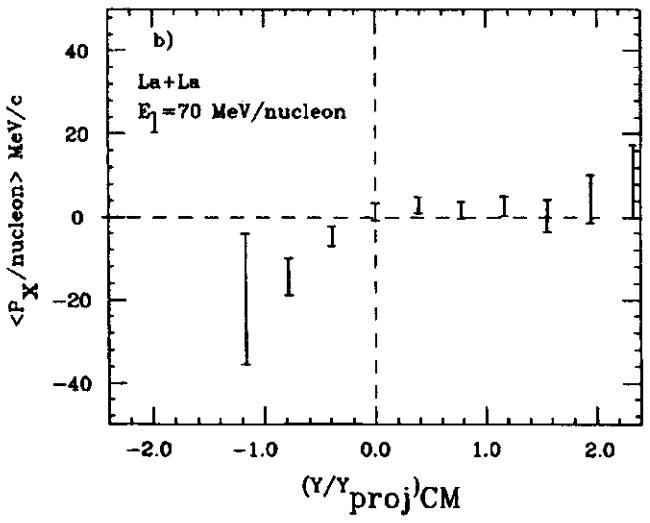

FIG. 2: Same as for Fig. 1, except E_{lab} = 70 MeV/nucleon.

Because of the way the observable is defined[4], however, the experimentally obtained transverse momentum would merely show a gradual decrease towards zero as the bombarding energy is lowered. We have attempted to observe this effect by deducing transverse momentum spectra for the reaction La + La at laboratory bombarding energies of 50, 70 and 130 MeV/nucleon.

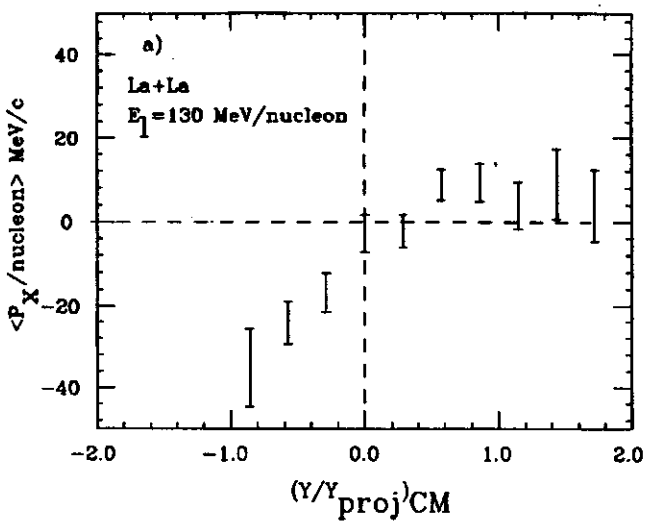

FIG. 1: Average center-of-mass transverse momentum projected upon the found reaction plane for E_{lab} = 130 MeV/nucleon. These data points have been corrected for the streamer chamber azimuthal detection efficiency variation.[4]

The work was performed at the Lawrence Berkeley Laboratory Streamer Chamber Facility using charge-coupled device (CCD) cameras and fully automated data analysis techniques.[5] The data sets are based upon central collision triggers and consist of 367 events at 130 MeV/nucleon, 946 events at 70 MeV/nucleon and 177 events at 50 MeV/nucleon.

Figures 1, 2 and 3 show the average center-of-mass projected transverse momentum spectra for each of the beam energies. It is seen that the average value of the transverse momentum near the projectile rapidities does decrease as the beam energy falls from 130 to 50 MeV/nucleon. The statistical accuracy is reduced in the backward hemisphere for each energy because of the reduced efficiency of reconstructing the spatial tracks of low energy fragments. Preliminary analysis on the statistical and systematic uncertainties yields the average transverse momentum at projectile rapidity values of Table I. Such

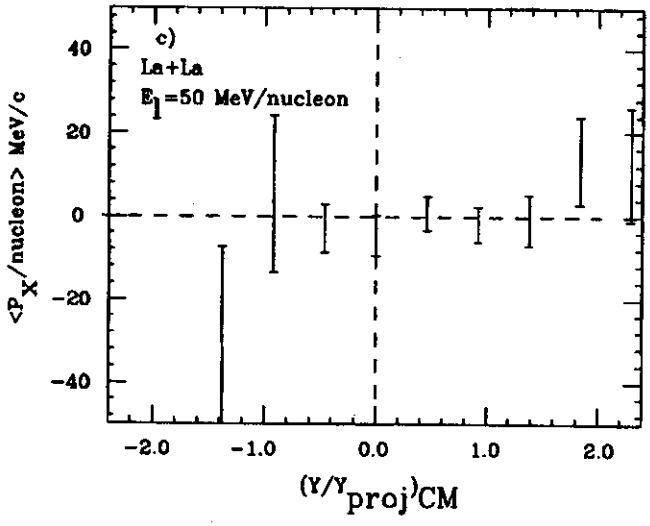

FIG. 3: Same as for Fig. 1, except E_{lab} = 50 MeV/nucleon.

values appear to be consistent with the predictions of Molitoris[1] on the nature of the energy dependence of intermediate energy transverse momentum spectra.

TABLE I: Average values of the plateau region of the projected transverse momentum near beam rapidity. The quoted uncertainties contain statistical and systematic contributions.

E_{lab} (MeV/nucleon)	<px/nucleon> (MeV/c)
50	0.7± 3.1
70	2.4 +1.7, -2.2
130	8.0 ± 3.8

References

a. University of South Carolina.

b. University of Michigan.

1. J. Molitoris, D. Hahn and H. Stöcker, Nucl. Phys. A447, 13c (1986).

2. G.F. Bertsch, W.G. Lynch and M.B. Tsang, Phys. Lett. B189, 384 (1987).

3. M.B. Tsang *et al.*, Phys. Rev. Lett. 52, 559 (1986).

4. P. Danielewicz and G. Odyniec, Phys. Lett. 157B, 146 (1985).

5. S. Angius *et al.*, Nucl. Instrum. Methods A273, 283 (1988).

Event Topography Analysis: Sequential Versus Multifragment Emission

D.A. Cebra, J. Clayton, S. Howden, J. Karn, A. Nadasen, C.A. Ogilvie, A. Vander Molen, G.D. Westfall, W.K. Wilson, and J. Winfield

It has been observed that in nuclear collisions at intermediate energy (20 MeV/n to 200 MeV/n) composite systems can break up into several intermediate mass fragments (IMF's = Z≥ 3). However, the dynamics of this disassembly process is yet to be determined. The observed mass and multiplicity distributions can be reproduced by models simulating either a simultaneous multifragmentation or a sequential decay process.

It has been proposed that by studying multiparticle correlations, one can distinguish between these two processes[1]. For example, the shape of the momentum distribution of the outgoing fragments, or the event topography, is formed during the emission stage of a reaction, and thus will be influenced by the dynamics of the breakup. One expects that simultaneous multifragmentation should have no preferred axis in the center of mass frame and therefore a spherical shape would result. On the other hand, sequential emission should lead momentum distribution that is elongated in one axis due to the kinematical constraints of the binary decays.

We have studied the system 35 MeV/n Ar+V using the MSU 4 π array and have used the technique of event topography analysis to determine the breakup process. In this technique, one first transforms the observed event into the rest frame of the center-of-mass of the projectile and target nuclei and then constructs a kinetic-flow tensor

$$F_{ij} = \sum \frac{p_i^{(n)} p_j^{(n)}}{2m_n}$$

where $p_i^{(n)}$ denotes a momentum component of the nth particle and m_n is its mass. One uses the ordered magnitudes of the eigenvectors of this tensor, $t_1 < t_2 < t_3$, to define three reduced quantities

$$q_i = \frac{t_i^2}{\sum_{j=1}^{3} t_j^2}$$

From these, one can determine the sphericity, $S = \frac{3}{2}(1 - q_3)$, and the coplanarity, $C = \frac{1}{2}\sqrt{3}(q_2 - q_1)$.[1,2] The relative values of these two parameters determine the shape of the spheroid that best approximates the envelope of the outgoing momentum vectors of the fragments.

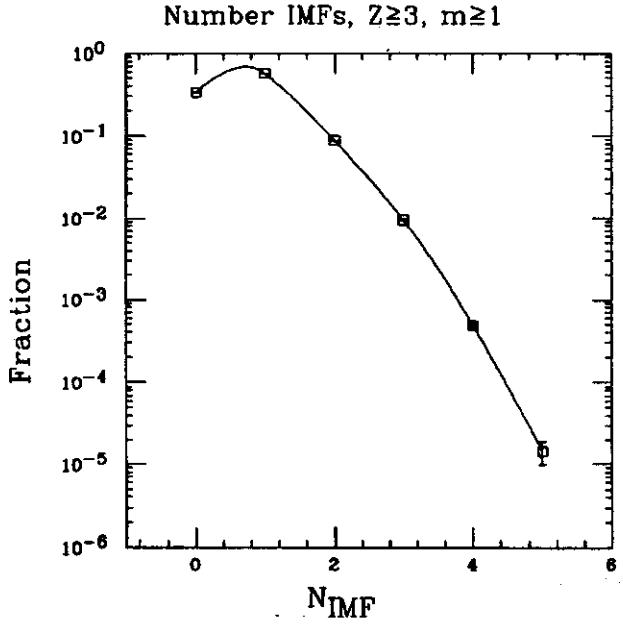

FIG. 1: Complex fragment multiplicity from 35 MeV/n Ar+V.

In Fig. 1, the multiplicity distribution of IMFs is displayed from events triggered with multiplicity greater or equal to one. Note that about 1% of the observed events have three or more detected IMFs. All of the observed particles are used in the following analysis, which means that the light fragments can dominate the measured event shapes simply due to their higher observed multiplicity.

In a previous comparison of the predicted event topography between simultaneous multifragmentation and sequential breakup, data from simulations was used and it was assumed that all produced particles could be detected. All detector systems, however, place some bias on the data. For the MSU 4π array, these biases include non-detection of neutral particles, minimum energy thresholds, and finite granularity. Before one can compare the data to a model, one must understand the effect that these biases impose on the distributions. Therefore, we have filtered the simulated events through a software replica of our detector system. After filtering, it is still possible to distinguish between the two proposed processes predicted by the models.

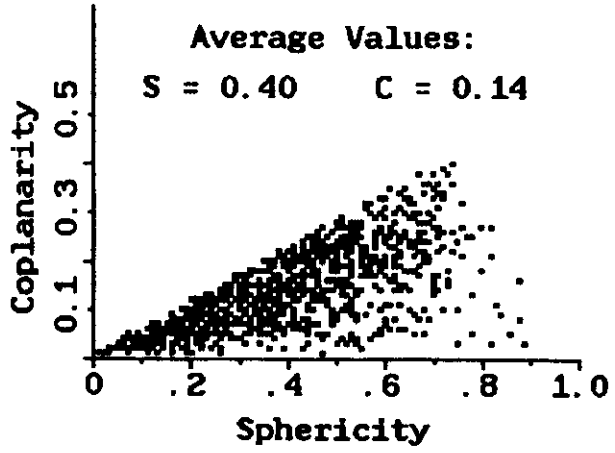

FIG. 2: Predictions from a simulation (FREESCO) of simultaneous multifragment emission filtered through the acceptance of the MSU 4π array.

In Fig. 2, the predicted distribution arising from a simultaneous multifragmentation is displayed. From this reaction process, one expects the topography of an average event to resemble a triaxial spheroid (S_{av} = 0.40, C_{av} = 0.14). To reproduce this process we used FREESCO, which is an explosion and evaporation code.[3]

The predicted distribution for a sequential breakup process is displayed in Fig. 3. The average shape for these events is more two-dimensional and more elongated (S_{av} = 0.25, C_{av} = 0.10) than the previous model. This simulation assumed an initial system of 80 nucleons with an excitation energy of 5.0 MeV/n. The data was provided by Lopez and then filtered.

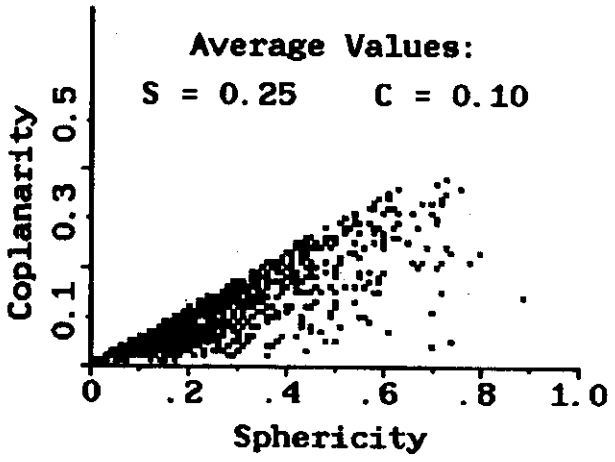

FIG. 3: Predictions from a simulation of a sequential breakup filtered through the acceptance of the MSU 4π array.

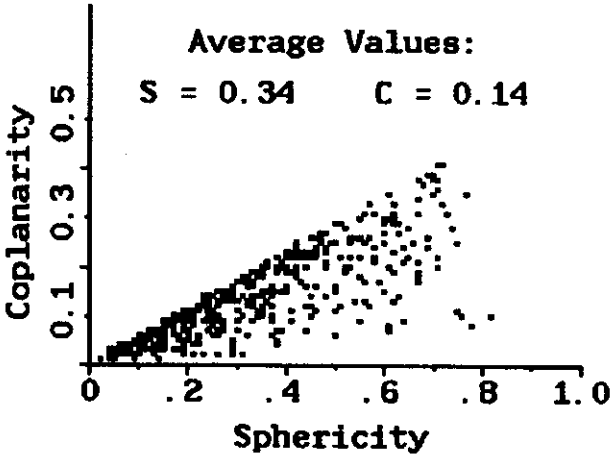

FIG. 4: Event topography distribution from 35 MeV/n Ar+V, gated on central impact parameters as determined by the intermediate rapidity charge.

The shape distribution for the data acquired by the MSU 4π array is shown in Fig. 4. The events used for this analysis have been gated on impact parameter, and only the most central ($b < 0.2\, b_{max}$) collisions have been used for this analysis. The determination of the centrality was made on an event-by-event basis, and is based on the detected charge multiplicity of fragments in the mid-rapidity range ($0.75y_{targ} < y_{frag} < 0.75y_{proj}$) in the center-of-mass. This range has been demonstrated to be a reliable measure of impact parameter for our detection system.[4] The centroid of the event topography distribution (S_{av} = 0.34, C_{av} = 0.14) falls between the two predicted values; however, the distribution of the experimental data resembles more

closely that predicted for the simultaneous multifragmentation than that for sequential decay. One would have expected a much flatter, more elongated shape from a sequential decay process.

We can conclude from this analysis that neither the simple sequential decay as calculated by Lopez nor the simultaneous multifragmentation of FREESCO accurately reproduce the decay dynamics for these events. The data suggest that there is either a mixing of processes or an averaging of events that could be characterized by one or the other model.

References

1. J. Lopez and J. Randrup, Nucl. Phys. A491, 477 (1989).

2. M. Gyulassy, K.A. Frankel and H. Stöcker, Phys. Lett. 110B, 185 (1982).

3. G. Fai and J. Randrup, Computer Phys. Commun. 42, 385 (1986).

4. C. Ogilvie *et al.*, Phys. Rev. C, to be published (1989).

Reaction Filters:
Charged-Particle Multiplicity and Linear Momentum Transfer

M.B. Tsang, Y.D. Kim, N. Carlin, Z. Chen, R. Fox, C.K. Gelbke, W.G. Gong, W.G. Lynch, T. Murakami, T.K. Nayak, R.M. Ronningen, H.M. Xu, F. Zhu, L. Sobotka,[a] D. Stracener,[a] D.G. Sarantites,[a] Z. Majka,[b] V. Abenante,[a] and H. Griffin[c]

For nucleus-nucleus collisions at intermediate energies, E/A≈20-200 MeV, particle emission from the early stages of the reaction can exhibit a complex interplay of dynamic and geometric effects.[1,2] Inclusive experiments determine only impact-parameter-averaged quantities. The resulting loss of information can lead to ambiguous interpretations, which could be overcome by employing suitable reaction filters capable of selecting specific classes of collisions. Such filters are particularly useful if they can be used to select well defined narrow ranges of impact parameters.

A number of different techniques have been explored. The folding angle, Θ_{ff}, between coincident fission fragments provides information about the linear momentum transfer to fissionable heavy reaction residues.[3-10] Folding angle measurements can discriminate between peripheral, quasi-elastic collisions, and central, fusion-like reactions.[4,5,9,10] An alternative technique employs neutron multiplicity measurements.[11,12] For the $^{20}Ne+U$ reaction at E/A=14.5 MeV, the measured neutron multiplicity was found to exhibit a monotonic and nearly linear dependence on folding angle,[11] indicating a close relation between these two kinds of reaction filters, at least at low incident energies.

Existing 4π neutron detectors are mostly sensitive to low-energy neutrons emitted in the statistical decay of fully equilibrated reaction products. Hence, the measured neutron multiplicity is closely related to the amount of energy deposited into equilibrated degrees of freedom. Since energies and angles of the emitted neutrons are not measured, other details of the reaction remain undetermined, e.g. the orientation of the reaction plane or the transverse momentum of the emitted particles.[13]

Charged-particle detector arrays[14] can overcome such limitations and provide information about the multiplicities of energetic emissions for which 4π neutron detectors become inefficient. For low incident energies, the multiplicity of charged particles emitted statistically to backward angles will largely reflect the excitation energies of the nearly equilibrated reaction residues. The multiplicities of charged particles emitted to forward angles, on the other hand, are mainly dominated by non-equilibrium processes. With increasing energy, the multiplicities of these non-equilibrium emissions should reflect to an increasing degree the impact-parameter-dependent geometry or "participant volume" characteristic of the early stages of the collision.[15] At intermediate energies, both equilibrium and non-equilibrium emissions are present.

The multiplicities arising from non-equilibrium emission are small,[16] and the sensitivity of any charged-particle array to either process may depend strongly upon the angular range subtended by the device. We have performed a cross calibration of charged-particle multiplicity filters for intermediate energy collisions, through an experimental investigation of the relationship between charged-particle multiplicities and fission-fragment folding angles for the reactions $^{36}Ar+^{238}U$ at E/A=35 MeV and $^{14}N+^{238}U$ at E/A=50 MeV.

The experiment was performed at the NSCL. A 3×6-mm^2 spot target of $^{238}UF_4$ (areal density≈400 μg/cm^2), evaporated on a carbon foil (areal density≈50 μg/cm^2), was irradiated by ^{36}Ar and ^{14}N ions of E/A=35 and 50 MeV, respectively. Charged particles, Z=1-8, were detected with the "Dwarf Ball-Wall" array developed at Washington University.[17] From the original array of 105 phoswich detectors, seven detectors were removed to provide openings for the target-holding mechanism and for the passage of fission fragments; two additional detectors malfunctioned during the experiment. The remaining total of 96 functional phoswich detectors covered a solid angle corresponding to 85% of 4π.

Particle identification was achieved by integrating the photomultiplier anode current over three different time gates. A fast gate (0→ 50 ns) was used to measure the light emitted by the plastic scintillator foils. The total charge in this gate was combined with the charge in a slow time gate (50→650 ns) to obtain elemental identification up to about $Z \approx 6$. The second time gate was also used to determine the energy of the detected particle and was combined with a third time gate (1→2 μs) to obtain pulse shape discrimination for particles with $Z \leq 2$.

Fission fragments were detected with two *X-Y*-position-sensitive parallel-plate multiwire detectors with tapped delay-line readout,[18] covering angular ranges of $\Theta_1 = 36°\text{-}116°$, and $\Theta_2 = -(39°\text{-}89°)$ in the reaction plane. In the off-line analysis, energy thresholds of 12 and 18 MeV for hydrogen and helium nuclei, respectively, were used for detectors located at $\Theta > 35°$. For $\Theta < 35°$, the thresholds were 20 MeV for both hydrogen and helium. For heavier particles, the fragment energy thresholds were $E/A \approx 6\text{-}9$ MeV and $E/A \approx 2\text{-}3$ MeV for detectors located at $\Theta < 35°$ and $\Theta > 35°$, respectively.

Figure 1 shows two-dimensional contour diagrams of folding angle Θ_{ff} versus measured charged-particle multiplicities. (These raw multiplicities are not corrected for efficiency losses due to detection thresholds and incomplete solid-angle coverage; therefore, they are slightly smaller than the true charged-particle multiplicities.) The left- and right-hand panels show data for the $^{14}N+^{238}U$ and $^{36}Ar+^{238}U$ reactions, respectively. For orientation, the upper scales give the linear momentum transfer, $\Delta P/P$, to the heavy reaction residue in units of the projectile momentum, P, assuming symmetric fission of the compound nucleus. The upper panels show the total multiplicities, M, measured with the entire array (covering the angular range of $\Theta \approx 5°\text{-}170°$). The center panels show the number of particles detected with the "Dwarf Ball" (covering the angular range of $\Theta \approx 35°\text{-}170°$) and the lower panels show the number of particles detected with the "Dwarf Wall" (covering the angular range of $\Theta \approx 5°\text{-}35°$).

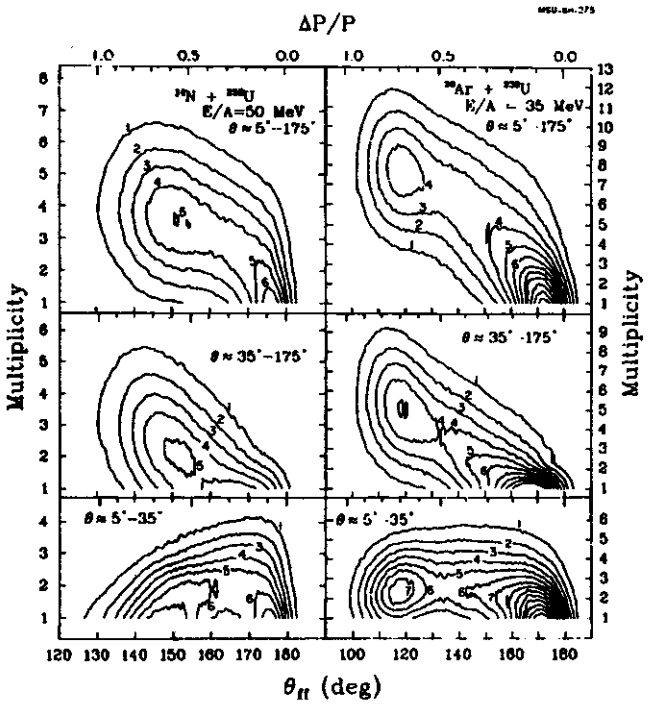

FIG. 1: Measured correlation between charged particle multiplicity and folding angle for the $^{14}N+^{238}U$ reaction at E/A = 50 MeV (left-hand side) and for the $^{36}Ar+^{238}U$ reaction at E/A = 35 MeV (right-hand side). The angular range over which the charged particles are detected is indicated for each panel. The numbers of events (divided by a factor 1,000) for individual contours are given in the figure.

For both reactions, the average multiplicity of charged particles emitted over the entire angular range ($\Theta \approx 5°\text{-}170°$) increases monotonically with increasing linear momentum transfer to the heavy reaction residue. This dependence is qualitatively similar to the monotonic relation between neutron multiplicity and folding angle which has been established for reactions at lower incident energies.[11,12] For the $^{36}Ar+^{238}U$ reaction, the dependence of the average multiplicity on folding angle is similar to the results obtained for a similar reaction at a slightly lower energy. A nearly linear correlation between multiplicity and linear momentum transfer is observed for charged particles emitted at intermediate and large angles ($\Theta \approx 35°\text{-}170°$). In contrast, the multiplicity of charged particles emitted at forward angles ($\Theta \approx 5°\text{-}35°$) is nearly independent of the linear momentum transfer to the heavy reaction residue.[6] At least for the present reactions, the multiplicities detected in forward arrays cannot be used to select violent projectile-target interactions in which large amounts of energy and/or momentum are dissipated.

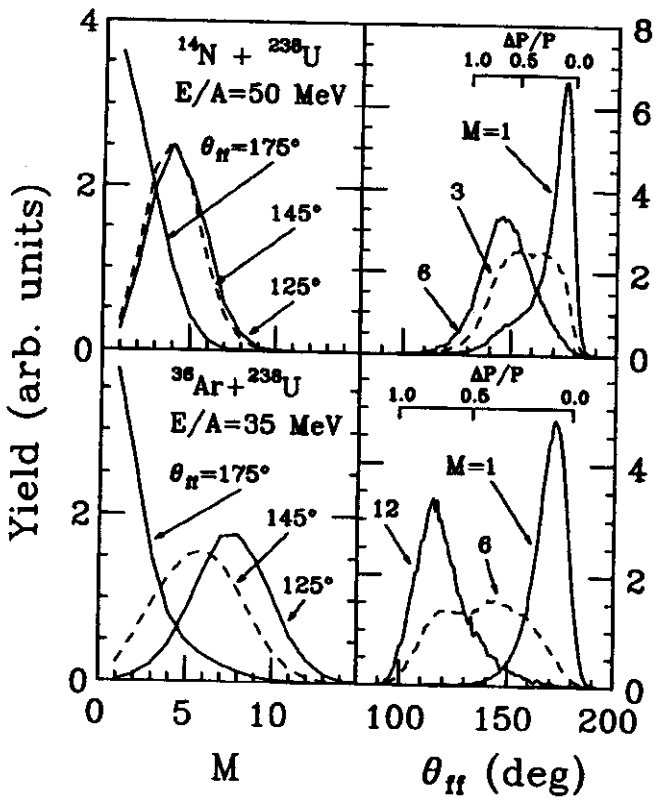

FIG. 2: Gated multiplicity (left-hand panels) and folding angle (right-hand panels) distributions measured for the reactions ^{14}N+^{238}U at E/A=50 MeV (upper part) and ^{36}Ar+^{238}U at E/A=35 MeV (lower part). The distributions for each panel are normalized to the same integrated yield. The gates on folding angle, θ_{ff}, are 1° wide; their centers are indicated in the left-hand panels. The gates on multiplicity, M, are indicated in the right-hand panels.

Charged-particle multiplicity, as well as folding angle measurements, represent reaction filters of finite resolution. Even for the ideal case of formation and decay of a composite nuclear system with unique spin, excitation energy, and recoil momentum, multiplicity and folding angle distributions have finite widths. The widths of folding angle distributions reflect the finite widths of the mass and kinetic energy distributions of the fission fragments, as well as smearing from light particle evaporation. For more energetic collisions, additional broadening can be caused by the emission of intermediate mass fragments.[9] The widths of charged particle multiplicity distributions reflect the stochastic nature of neutron and charged-particle emission mechanisms. Particularly at lower energies, where the charged-particle multiplicities are small, statistical fluctuations in the multiplicities can be comparable to the mean values, and the selectivity of charged-particle multiplicities as reaction filters can be reduced.

The widths of various gated distributions are shown in Fig. 2. The upper and lower sections show data for the ^{14}N+^{238}U and the ^{36}Ar+^{238}U reactions, respectively. The left-hand panels show distributions for total charged particle multiplicity gated by folding angle intervals, 1° wide and centered at the indicated angles. The right-hand panels show folding angle distributions measured for different total charged particle multiplicities, M = 1, 3, 6 for the ^{14}N+^{38}U reaction and M = 1, 6, 12 for the ^{36}Ar+^{38}U reaction. The high-multiplicity gates (M=6 for ^{14}N+^{38}U and M=12 for ^{36}Ar+^{38}U) represent cuts in the tails of the charged-particle multiplicity distributions, at values approximately 50% larger than the most probable multiplicity observed for fusion-like collisions (see left-hand panels, or Fig. 1).

Charged-particle multiplicity distributions gated by large folding angles, $\theta_{ff} \approx 175°$, are clearly peaked at M≤1. However, they exhibit remarkably long tails extending to high multiplicities. Multiplicity distributions gated by small folding angles (or fusion-like collisions) are peaked at M≈4 and 8 for the ^{14}N+^{238}U and ^{36}Ar+^{238}U reactions, respectively. They are rather broad, indicating significant fluctuations of the number of emitted charged particles. There is considerable overlap between the multiplicity distributions gated by very different folding angles.

Folding angle distributions gated by low- (high-)charged particle multiplicities are peaked at large (small) folding angles, respectively. The widths of these distributions are very similar to the widths measured for the out-of-plane distributions of fission fragments selected by the same multiplicity gates, indicating that these gates do not introduce significant broadening beyond the intrinsic resolution of the folding angle technique. In contrast, folding angle distributions gated by intermediate charged-particle multiplicities (M=3 for ^{14}N+^{238}U and M=6 for ^{36}Ar+^{238}U) are significantly broader, indicating that such multiplicity gates are less selective.

References

a. Department of Chemistry, Washington University, St. Louis, MO 63130

b. Department of Chemistry, University of Michigan, Ann Arbor, MI 48109

c. Washington University[a], on leave from Institute of Physics, Jagellonian University, PL-30-059 Cracow, Poland

1. A.A. Amsden *et al.*, Phys. Rev. Lett. 35, 905 (1975).

2. G.F. Bertsch *et al.*, Phys. Lett. 189B, 384 (1987).

3. T. Sikkeland *et al.*, Phys. Rev. 125, 1350 (1962).

4. B.B. Back *et al.*, Phys. Rev. C22, 1927 (1980).

5. T.C. Awes *et al.*, Phys. Rev. C24, 89 (1981).

6. D. Jacquet *et al.*, Phys. Rev. C32, 1594 (1985).

7. G. Bizard *et al.*, Nucl. Phys. A456, 173 (1986).

8. Y. Patin *et al.*, Nucl. Phys. A457, 146 (1986).

9. M. Fatyga *et al.*, Phys. Rev. Lett. 58, 2527 (1987).

10. Z. Chen, Nucl. Phys. A473, 564 (1987).

11. J. Galin, Nucl. Phys. A447, 519c (1985).

12. M. Morjean *et al.*, Phys. Lett. B203, 215 (1988).

13. P. Danielewicz and G. Odyniec, Phys. Lett. 157B, 146 (1985).

14. A. Baden *et al.*, Nucl. Instrum. Methods 203, 189 (1982).

15. G.D. Westfall *et al.*, Phys. Rev. Lett. 37, 1202 (1976).

16. G.D. Westfall *et al.*, Phys. Lett. 116B, 118 (1982).

17. D.G. Sarantites *et al.*, Nucl. Instrum. Methods A264, 319 (1988). This paper details an early version of the device which used fast-slow plastic phoswich elements. The device was later modified by using plastic-CsI(Tl) phoswich elements. These modifications are the subject of a forthcoming publication.

18. A. Breskin *et al.*, Nucl. Instrum. Methods 221, 363 (1984).